공학박사학위논문

전체 공기저항 감소를 위한 전후대칭열차의 전두부 최적형상 연구

A Study on Optimum Nose Shape of a Front-Rear Symmetric Train for the Reduction of the Total Aerodynamic Drag

2013 년 8 월

서울대학교 대학원
기계항공공학부
곽 민 호

전체 공기저항 감소를 위한
전후대칭열차의 전두부 최적형상 연구

A Study on Optimum Nose Shape of
a Front-Rear Symmetric Train
for the Reduction of the Total Aerodynamic Drag

지도교수 이 동 호

이 논문을 공학박사 학위논문으로 제출함

2013 년 4 월

서울대학교 대학원

기계항공공학부

곽 민 호

곽민호의 공학박사 학위논문을 인준함

2013 년 6 월

위 원 장 : ____________________

부위원장 : ____________________

위　　원 : ____________________

위　　원 : ____________________

위　　원 : ____________________

Abstract

A Study on Optimum Nose Shape of a Front-Rear Symmetric Train for the Reduction of the Total Aerodynamic Drag

Minho Kwak
School of Mechanical and Aerospace Engineering
Seoul National University

A high-speed train uses two symmetrically corresponding shaped power cars at both ends. Consequently, the same nose shape plays a role as a leading part and a role as a trailing part in one train at the same time. Thus the existing model of the optimized first car nose shape which does not consider the entire train is not sound in terms of the aerodynamic drag. Also, while accurate simulation of the wake area behind the train is very significant for the design optimization of the three-dimensional shape, accuracy of previous studies has been limited by their train shapes and boundary conditions. Therefore, it is necessary to consider the entire train including the first car nose and the last car nose and especially accurate simulation of the wake area for the optimization of the shape design of a three-dimensional symmetric train in order to reduce the total aerodynamic drag.

In this dissertation, two nose shape optimizations of the front-rear symmetric train are performed with no constraint for the reduction of the total aerodynamic drag and with the constraint of the optimized cross-sectional area distribution for the reduction of the total aerodynamic drag and the mi-

cro-pressure wave respectively. The three-dimensional train nose shape is constructed through Vehicle Modeling Function and a viscous compressible flow solver is adopted with unstructured meshes to predict the aerodynamic drag. The two optimizations are respectively performed under consideration of two cases – for the total aerodynamic drag of the entire train and for the aerodynamic drag of the first car only by the previous method for the reduction of design time. Also, an Artificial Neural Network is constructed with the experimental points extracted by Maxi-min Latin Hypercube Sampling method.

In the unconstrained optimization, it was found that the total aerodynamic drag of the entire train with the optimized shape for the entire train was reduced by 5.8% when compared to the unconstrained base model, whereas that with the optimized shape for only the first car is changed little. On the other hand, in the constrained optimization, the total aerodynamic drag of the entire train with the optimized shape for the entire train was effectively reduced by 15.3 % when compared to that of the constrained base model while that with the optimized shape for only the first car is increased by 9.7% on the contrary.

The low-risen and long vertical nose shape of the unconstrained optimum weakens the whirled flow around the nose tip. On the other hand, the low-risen and wide horizontal nose shape of the constrained optimum weakens the up-wash flow and vortices behind the blunt nose. Both shape characteristics reduce the overall aerodynamic drag of each base model.

Therefore, the three dimensional modeling is very necessary for design optimization of the actual front-rear symmetric train in that the wake area behind the train must be simulated as accurately as possible. In doing so, Vehicle Modeling Function is a valuable tool in successful three-dimensional shape

optimization since it has no modeling constraint to functionalize three-dimensional shape thus efficiently enables the various models of the three-dimensional train shape. Also, it is required to design symmetrically identical both noses in order to reduce the total aerodynamic drag.

Key Words : Front-rear symmetric train, 3-D Nose shape, Wake area simulation, Vehicle Modeling Function, Aerodynamic drag, Design optimization

Student Number : 2006-23068

Table of Contents

Nomenclatures

English Symbols

A	: Surface area
A(x)	: Cross-sectional area of train nose in longitudinal direction
A_1	: Curvature of the front part of the basic curve in Vehicle Modeling Function
A_2	: Curvature of the rear part of the basic curve in Vehicle Modeling Function
A_{FL}	: Curvature of the lower corner of the cross-section shape from a front view
A_{FU}	: Curvature of the upper corner of the cross-section shape from a front view
A_L	: Curvature of the lower nose curve from a side view
A_{ref}	: Maximum cross-sectional area of train body
A_T	: Curvature of the nose curve from a top view
A_{U1}	: Curvature of the 1st upper nose curve from a side view
A_{U2}	: Curvature of the 2nd upper nose curve from a side view
ANN	: Artificial Neural Network
C_D	: Aerodynamic drag coefficient
dA	: Differential surface area
E	: Total energy per unit mass
F	: Aerodynamic drag force
H	: Height of the basic curve in Vehicle Modeling Function
H_{CW}	: Height of the cockpit window
H_N	: Height of the point where upper nose curve and lower nose curve meet
k	: Turbulence kinetic energy
L	: Length of the basic curve in Vehicle Modeling Function
L_{LN}	: Length of the lower nose curve in the longitudinal direction
L_{UN}	: Length of the upper nose curve in the longitudinal direction
p	: Pressure

P_U : Change speed of the upper cross-section corner shape from front to rear

q : Heat flux

u : Fluid velocity in longitudinal direction

x_p : X coordinates of the starting point of the basic curve in Vehicle Modeling Function

X_{IN} : Length of the 1st upper nose curve in the longitudinal direction

v : Fluid velocity in lateral direction

V : Arbitrary control volume

V_t : Train speed

$\vec{v}$: Fluid velocity

VMF : Vehicle Modeling Function

w : Fluid velocity in vertical direction

z_p : Z coordinates of the starting point of the basic curve in Vehicle Modeling Function

Z_{IN} : Height of the 1st upper nose curve in the vertical direction

Greek Symbols

ρ : Fluid density

τ : Viscous stress tensor

ε : Dissipation rate

ω : Specific dissipation rate

Subscripts

CW : Cockpit Window

D : Drag

F : Front view

IN	: Interface
L	: Lower
N	: Nose
ref	: Reference
T	: Top view
U	: Upper

List of Tables

List of Figures

Chapter 1. Introduction

1.1 Aerodynamics of a High-Speed Train

Recently, innovative models of ultra-high-speed trains that are capable of speeds exceeding 350 km/h are being developed in advanced countries of the high-speed train field [1]. In South Korea, HEMU-430x, which is Korean next generation high-speed train under development, set a Korean record speed of 421.4km/h in April 2013. Because aerodynamic problems appeared more seriously as trains run even faster, much active research about aerodynamic phenomena is being conducted [2-5]. The various studies are conducted for the primitive geometry, a real train, numerical or experimental techniques, wake behind the train, and the ground effect [6-9].

One of the most serious aerodynamic problems is the aerodynamic drag in the open field. The aerodynamic drag takes much greater parts of the total running resistance as the train speed increases. When a train speed is about 500 *km/h*, about 90 % of a total resistance is caused by the aerodynamic drag [10]. The aerodynamic drag is also known to be proportional to the square of a train speed. Most of the running resistance of a train can be written as [11]

$$R = A + BV_t + CV_t^2 \tag{1.1}$$

In Eq. (1.1), V_t is the train speed and the running resistance is expressed as the polynomial of the train speed. Therefore, A stands for the rolling resistance, BV_t does the momentum resistance, and CV_t^2 does the aerodynamic drag. Because the last term is proportional to the square of the speed, the aerodynamic drag is the term that increases most as the train speed increases. Most of the resistance is the aerodynamic drag at the ultra-high-speed.

Another issue is micro-pressure waves at the tunnel exit, especially considering that the portion of the tunnel to the total line is extremely high in the mountainous countries such as Korea and Japan. The micro-pressure wave is created at the tunnel exit due to a train's piston movement against the air inside the tunnel, as shown in Fig. 1.1 [12,13]. The intensity of the micro-pressure waves is known to be proportional to the cube of the train speed [13]. Therefore the aerodynamic drag and the micro-pressure wave become more critical issues as a train's speed increases.

1.2 Effect of External Shapes on Train Aerodynamics

The aerodynamic drag and the micro-pressure wave are affected mainly by the external shape of a train [1,10]. Nose shapes, gaps between cars, extruding objects (i.e. pantograph), a maximum cross-sectional area, a surface area and underbody shapes (i.e. bogie) influences the aerodynamic drag, whereas nose shapes and the maximum cross-sectional area does the micro-pressure wave, as shown in Fig. 1.2. Therefore, most of all, the train's noses have the greatest effect on the aerodynamic drag and the micro pressure wave of a high-speed train.

The aerodynamic drag is mainly affected by three-dimensional shape of the first car nose and the last car nose. On the other hand, the micro-pressure wave is primarily influenced by the cross-sectional area distribution of the first car nose.

Pressure drag due to the first car nose and the last car nose is relatively small for a long train. It is known that the pressure drag is just 8-13% for 13-car train [14]. However, recent ultra-high-speed trains become shorter. The length of HEMU−430x (6-car train) is about 150m [15]. The length of MLX01 (3-car train), Japanese developing Magnetic Levitation Train, is about 80m [16]. Then, the pressure drag caused by the first car nose and the last car nose will be about 19−39% [14]. Therefore, the pressure drag will become more important issue on the aerodynamic drag of a high-speed train.

There are various countermeasures on the train itself for increasing aerodynamic drag. Underbody shape modification, Bogie cover, pantograph cover, gap cover, long noses, and nose shape optimization [1, 17-24].

1.3 Previous Research for Train Nose Shapes

There have been useful studies about train noses. Hosaka et al. applied the new nose shape to the existing MLX01 train to reduce its aerodynamic drag and proved its effects through the running test [16]. Heine et al. performed the wind tunnel tests to investigate aerodynamic influence of shape parameters of the train nose [25]. They checked that the aerodynamic drag can be significantly decreased with not only long and slender nose but also low-rise car bodies. Siclari et al. carried out numerical calculation for several nose shapes of Magnetic Levitation Vehicle based on the super ellipse nose shape [26]. Hemida and Krajnovic investigated the influence of the shape of the nose on the flow structures [27]. They found that the short nose simulation shows highly unsteady and three-dimensional flow around the nose yielding more vortex structures in the wake.

Various nose shape optimizations have been performed in consideration of external nose shapes. Lorriaux et al. optimized 2-dimensional nose shape with numerical solver and the genetic algorithm [28]. Kranknovic proposed the optimization procedure for the cross-wind stability of the first car nose and one for the aerodynamic drag reduction with vortex generators at the last car [29]. Vytal et al. optimized 2-dimensional nose shape to minimize both the aerodynamic drag and the aerodynamic noise [30]. Kwon et al. optimized the axi-symmetric nose shape to reduce both the aerodynamic drag and the micro-pressure wave [31]. Ku et al. carried out the two-stage design optimization of the nose shape for the micro-pressure wave and the aerodynamic drag [32,33]. They obtained first the optimized one-dimensional cross-sectional area distribution of the first car nose for the reduction of the micro-pressure wave, and then optimized the three-dimensional shape of the first car nose to reduce the aerodynamic drag maintaining the cross-sectional area distribution obtained during the first stage for the reduction of design time.

1.4 Dissertation Objectives and Outlines

The total aerodynamic drag is mostly influenced by the first car nose and the last car nose because the shape of both noses changes drastically, as shown in Fig. 1.3 [1]. However, the wake area behind the last car was not simulated appropriately in the previous studies. The wake area behind the two-dimensional shape is different from that behind the three-dimensional body. The ground cannot be simulated for the axi-symmetric body and the different wake area is induced by no ground simulation. Thus, the entire train including the first car nose and the last car nose has to be considered at the same time for the three-dimensional nose shape optimization of a front-rear symmetric train with the goal of reducing the total aerodynamic drag.

The aim of the present study is to obtain a three-dimensional optimum aerodynamic nose shape of a front-rear symmetric train to reduce the total aerodynamic drag [34]. Two optimizations are performed with no constraint for one objective and under the constraint of the optimized cross-sectional area distribution for two objectives respectively, as shown in Fig. 1.4. Using Vehicle Modeling Function, three-dimensional train models are constructed with and without the constraint of the cross-sectional area distribution optimized for the reduction of the micro-pressure wave in the previous research [2]. Because all the train models satisfy the constraint, they automatically show the minimum micro-pressure wave [2,13]. A viscous compressible flow solver is adopted with unstructured meshes to predict the aerodynamic drag. The nose shape optimizations are performed for the reduction of the total aerodynamic drag of the entire train and of only the aerodynamic drag of the first car respectively. The optimization results for the total aerodynamic drag are compared to those of the optimization for the aerodynamic drag of the first car by the previous method for the reduction of design time in both the unconstrained optimization and the constrained optimization.

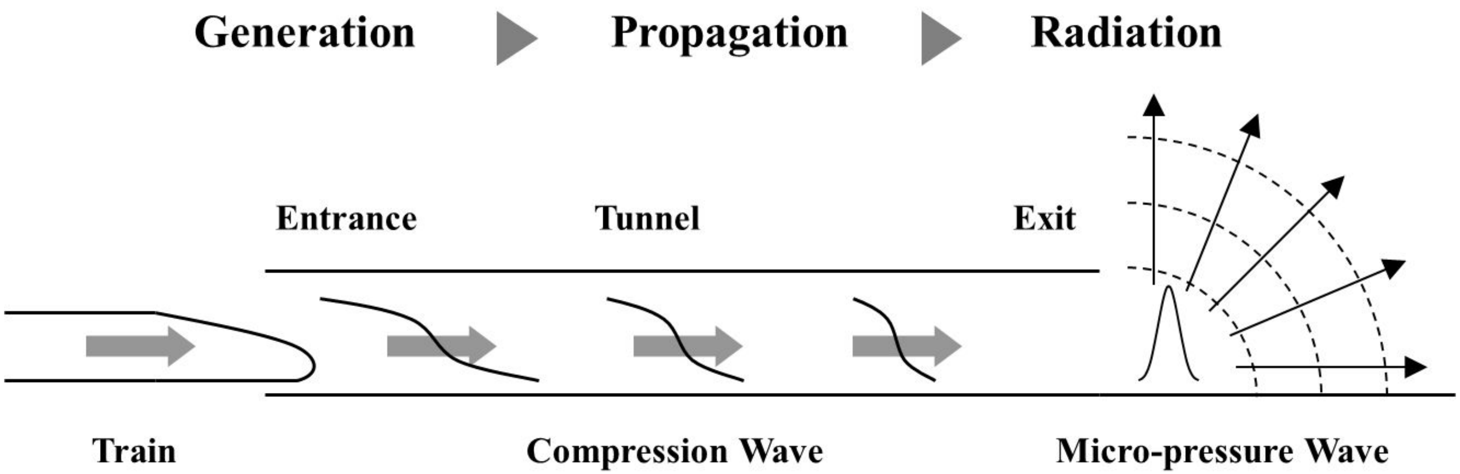

Fig. 1.1 Micro-pressure wave at a tunnel exit [13]

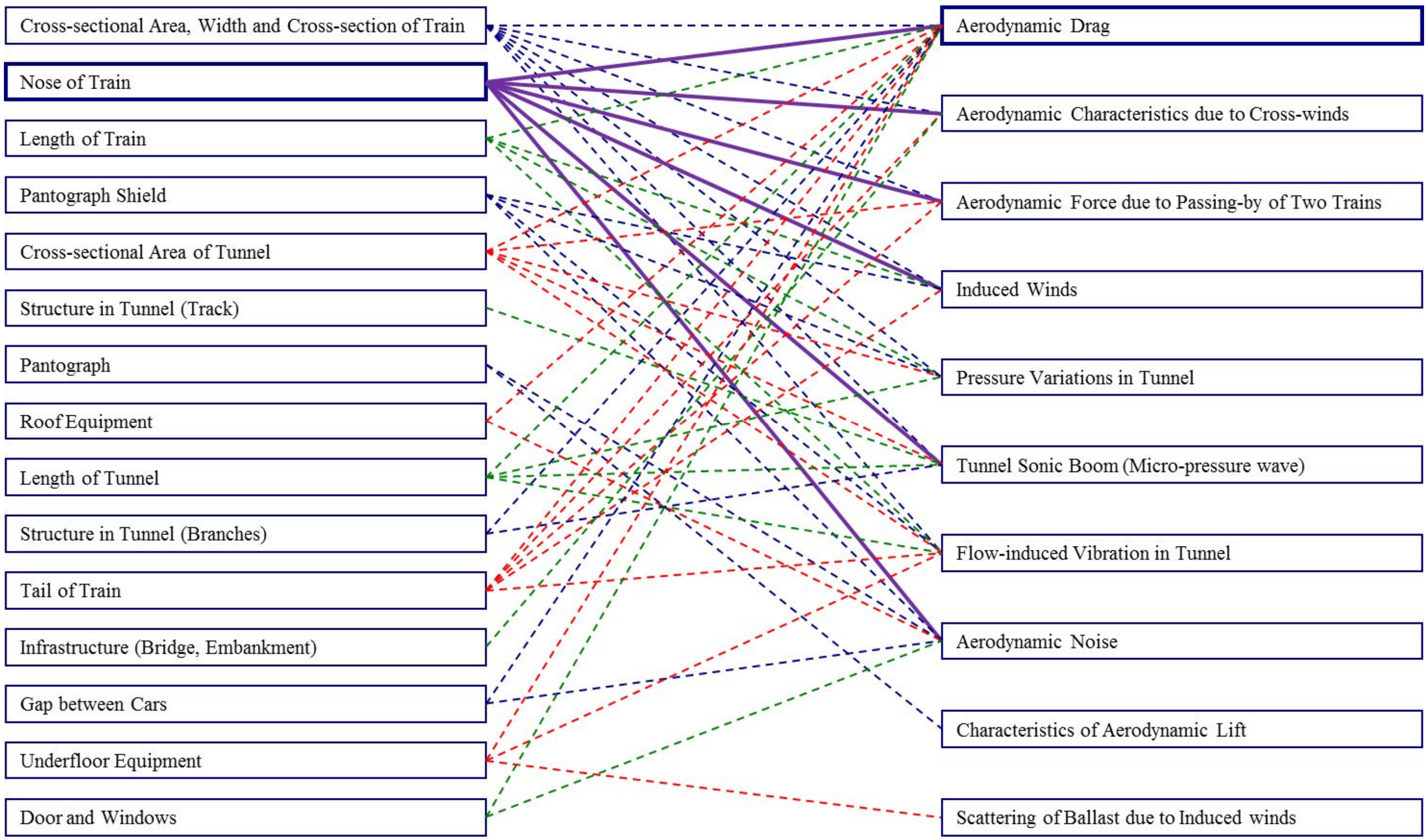

Fig. 1.2 External shapes of a train and related aerodynamic characteristics [1]

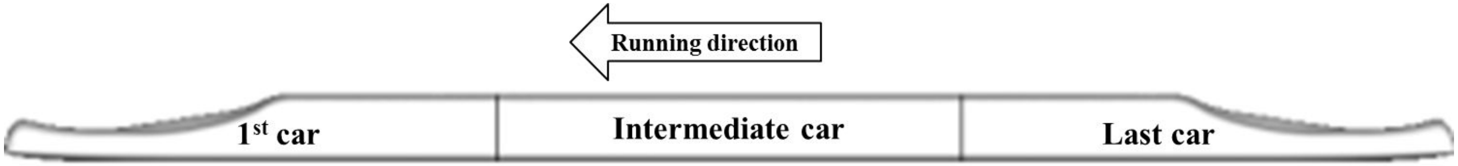

Fig. 1.3 A three-car streamlined model with no bogie wheel for a front-rear symmetric train model

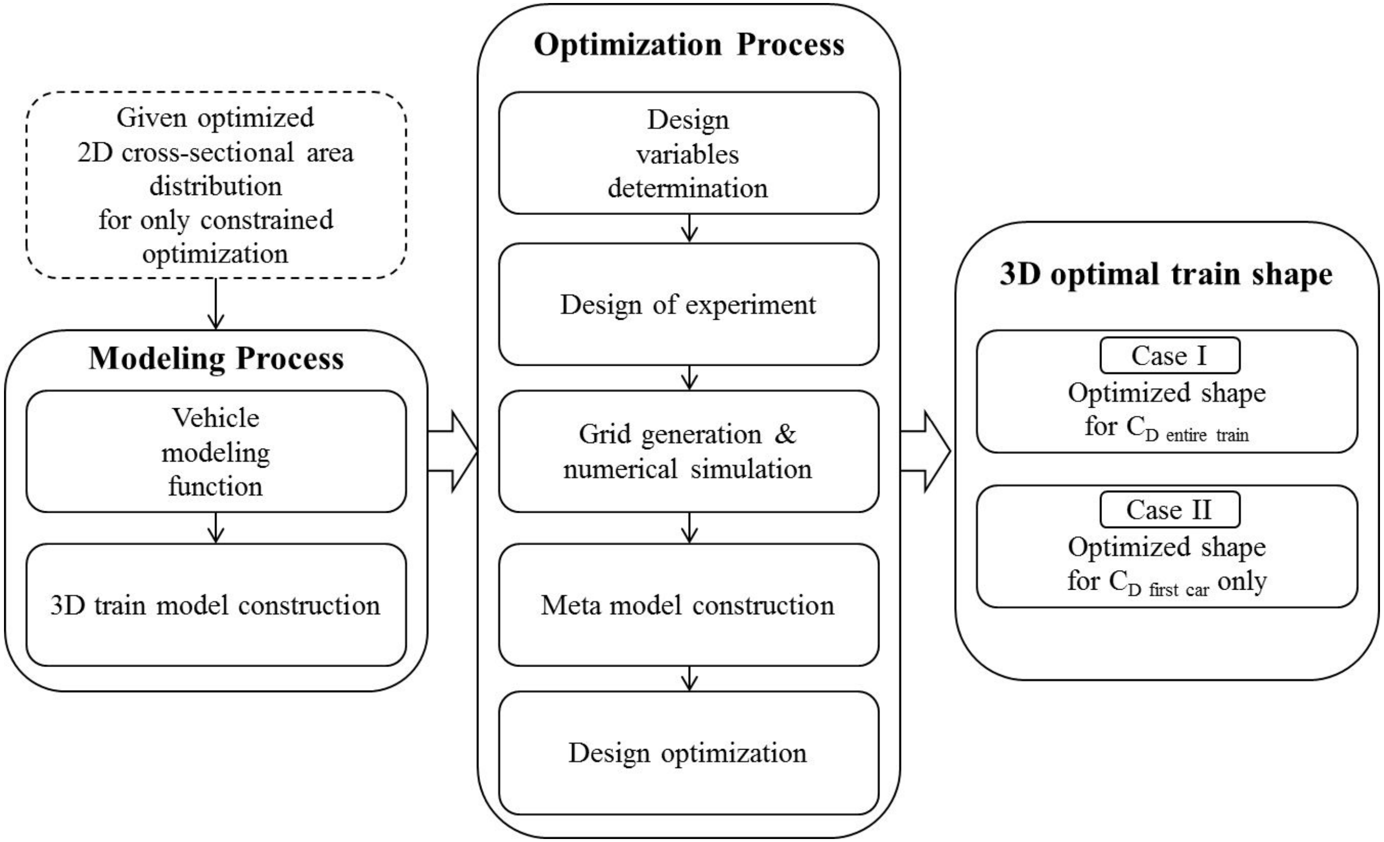

Fig. 1.4 Modeling and optimization processes of a high-speed train nose shape [32,33]

Chapter 2. Methodology

2.1 Numerical Method

2.1.1 Grid Generation for CFD Analysis

Unstructured grids are employed to form the grids of complex shapes. The grid geometry used for the numerical simulation is based on a three-car front-rear symmetric train. The computational domain is shown in Fig. 2.1. Ten boundary prism layers are applied to simulate the viscous flow in the vicinity of the train model more accurately, as shown in Fig. 2.2. Their total thickness is about 0.032m. All of the surfaces of the train model are a stationary wall and no slip condition was applied. To simulate the train's motion relative to the ground, a moving ground condition is applied to the only ground surface. The grid in the computational domain contains about 8 million cells for the unconstrained problem and 10 million cells for the constrained problem.

2.1.2 Methodology for CFD Analysis

In this study, the commercial CFD solver, ANSYS Fluent is used. The governing equations are the three-dimensional compressible Navier-Stokes equations, as shown below in vector form [35].

$$\frac{\partial}{\partial t}\int_{V}\vec{W}dV+\oint[\vec{F}-\vec{G}]\cdot dA=0 \tag{2.1}$$

,where $\vec{W}=\begin{bmatrix}\rho\\ \rho u\\ \rho v\\ \rho w\\ \rho E\end{bmatrix}$ $\vec{F}=\begin{bmatrix}\rho\vec{v}\\ \rho\vec{v}u+p\hat{i}\\ \rho\vec{v}v+p\hat{j}\\ \rho\vec{v}w+p\hat{k}\\ \rho\vec{v}E+p\vec{v}\end{bmatrix}$ $\vec{G}=\begin{bmatrix}0\\ \tau_{xi}\\ \tau_{yi}\\ \tau_{zi}\\ \tau_{ij}v_j+\vec{q}\end{bmatrix}$

A third-order monotone upstream centered scheme for conservation laws (MUSCL) and the Implicit Roe's Flux Difference Scheme (FDS) are used to solve the Navier-Stokes equations [36]. To model the turbulence for the flow in the vicinity of the train, the Shear Stress Transport (SST) $k-\omega$ model proposed by Mentor is used [37]. It is known for effectively blending the robust and accurate formulation of the $k-\omega$ model in the near-wall region with the free stream independence of the $k-\varepsilon$ model in the far field [35]. It is more accurate and reliable for a wider class of flows (e.g., adverse pressure gradient flows, airfoils, transonic shock waves).

Numerical simulations for all cases are performed at the operating speed of 500 km/h for a steady state. The Reynolds number which is based on the train's speed and the height of the train (3.52m) is about 3.36×10^{7}. For a comparison of the aerodynamic drag, C_D, the aerodynamic drag coefficient is used, as shown in Eq. (2.2).

$$C_D=\frac{F}{\frac{1}{2}\rho V^2 A_{ref}} \tag{2.2}$$

As shown in Fig. 2.3, the $C_D = \frac{\text{Aerodynamic force}}{\frac{1}{2}\rho v^2 \cdot \text{Area}}$ C_D history of the train model shows that the aerodynamic drag fluctuates periodically even after entering into a stable range, as the train shows strong three-dimensional and nonlinear flow phenomena. Therefore, the aerodynamic drag coefficients are averaged in the stable range for each case of the analysis.

2.1.3 Validation of the CFD Method

The numerical scheme in this study was validated through comparisons with previous experimental and numerical results, as shown in Fig. 2.4 [16]. Hosaka's running tests and numerical simulations were performed with MLX01, Japanese Maglev train under development. In Fig. 2.4, the present numerical results at a train speed of 500 km/h show good agreement with the previous experimental and numerical data for the surface pressure at the symmetric centerline surface of MLX01. Therefore, it can be said that the numerical scheme used in this study is sufficiently reliable.

2.2 Shape Modeling

2.2.1 Train Model

A three-car streamlined train model without any bogie wheel is used as the analysis model, as the trains become shorter and the portion of the pressure drag due to both noses increases as the operating speed of the train increases [14]. Especially for the analysis of this front-rear symmetric train, the first car nose and the last car nose are identical and always take on the same shape. The three-car front-rear symmetric train is composed of a first car, an intermediate car, and a last car, as shown in Fig. 2.5. The nose of the first car is the first car nose and that of the last car is the last car nose. Because the first car and the last car have the same shape, the first car nose and the last car nose are identical and always take on the same shape. The lengths of both noses are 5m, 10m, 15m respectively. The length of both end cars (the first car and the last car) is 25.9 m while the length of the intermediate car is 24.3m. The dimensions of the entire train model are 3.09 m (Width), 3.52 m (Height), and 76.1 m (Length). They are determined according to HEMU-430x, a Korean high-speed train under development [15]. The gap between the train model's bottom surfaces and the ground is 0.1 m according to the condition of MLX01 which is the developing Japanese MAGLEV train [16].

2.2.2 Vehicle Modeling Function

The Vehicle Modeling Function (VMF) proposed by Ku et al. is used for three-dimensional modeling in the present study [32,33]. First, Kulfan provided a new formula for the geometric representation of an airfoil [38,39]. Its mathematical form is following as

$$\zeta(\psi) = \psi^{N_1}(1-\psi)^{N_2} \cdot \sum_{i=0}^{N}\left[A_i \cdot \left(\frac{x}{c}\right)^i\right] + \psi \cdot \zeta_T \tag{2.3}$$

Where, ψ is x/c, ζ is z/c, ζ_T is $\Delta\zeta_{TE}/c$, and A_i is the coefficient of a general function that describes the unique shape of the geometry. This method ensures that the rounded nose and finite trailing edge thickness are expressed. It is very useful for an airfoil modeling. However, the ground vehicles have different configurations. Because they are blunter and more complicate, it is impossible to represent the ground vehicles by one curve.

Rho et al. applied this concept to automobiles by developing the section function and controlling the front and rear heights of a curve, as shown below [40].

$$Z\left(\frac{x}{c}\right) = \left(\frac{x}{c}\right)^{A_1}\left(1-\frac{x}{c}\right)^{A_2} \cdot S\left(\frac{x}{c}\right) + \left(1-\frac{x}{c}\right)Z_1 + \left(\frac{x}{c}\right)Z_2 \tag{2.5}$$

They developed the section function, $S(x/c)$ and adopt two last terms for control of the front and rear heights of a curve. The section function can produce discontinuous curves on the automobiles. However, this shape function for the automobile is not appropriate for the combination of several curves. Ku et al. expanded the original shape function by Kulfan differently to the train modeling as

$$Z(x) = \frac{H}{L^{A_1+A_2}}(x-x_p)^{A_1}[2L-(x-x_p)]^{A_2} + z_p \tag{2.6}$$

They let a starting point of a curve changeable and made the combination of several curves possible. This shape function for the three-dimensional train modeling is called the Vehicle Modeling Function [32,33,41]. There are six basic parameters in Eq. (2.6), as shown in Fig. 2.6. The x_p and z_p are the coordinates of the starting point, L and H are the length and height, respectively. These four variables are concerned with the scale and the position of a curve. Two exponents, A_1 and A_2, are related with the bluntness of the curve at the front and the rear parts of the basic curve.

To represent a three-dimensional nose shape, the vehicle modeling function is initially applied to each two-dimensional shape such as the side view, top view, and cross-section shape. After the two-dimensional shapes from a side view and a top view are produced first, through defining the cross-section shapes, the three-dimensional shape can be formed, as shown in Fig. 2.7. The attached parts are also expressed as a similar way and added to the main three-dimensional body without any discontinuous point.

For two-dimensional side view shape, the nose shape is classified into a one-box model and a two-box model [32]. For the one-box model, the side view shape of the nose can be represented by one vehicle modeling function, whereas two vehicle modeling functions are required for two-box model. In this study, the two-box model is used for the box type, as shown in Fig. 2.8-(a).

The two-dimensional side view and top view shapes are defined by the vehicle modeling function of Eq. (2.6). The side view shape can be expressed in Eq. (2.7)-(2.10), and is shown in Fig. 2.8-(a) [32]. An upper nose of two-box model from a side view is expressed as

$$Z_{SU}(x)=\begin{cases}\dfrac{H_E-H_N}{L_E^{A_1+A_2}}x^{A_1}(2L_E-x)^{A_2}+H_N & (0\le x\le L_E)\\ \dfrac{H_T-H_E}{(L_{NU}-L_E)^{A_1+A_2}}(x-L_E)^{A_1} & \\ \times[(2L_{NU}-L_E)-(x-L_E)]^{A_2}+H_E & (L_E\le x\le L_{NU})\\ H_T & (L_{NU}\le x\le L_T)\end{cases} \tag{2.7}$$

A lower nose from a side view is following as

$$Z_{SL}(x)=\begin{cases}\dfrac{H_{EXT}-H_N}{L_{NT}^{A_1+A_2}}x^{A_1}(2L_{NT}-x)^{A_2}+H_N & (0\le x\le L_{NL})\\ 0 & (L_{NL}\le x\le L_T)\end{cases} \tag{2.8}$$

where,

$$Z_{SL}(L_{NL})=\frac{H_{EXT}-H_N}{L_{NT}^{A_1+A_2}}L_{NL}^{A_1}(2L_{NT}-L_{NL})^{A_2}+H_N=0 \tag{2.9}$$

$$\therefore H_{EXT}=-H_N\frac{L_{NT}^{A_1+A_2}}{L_{NL}^{A_1}(2L_{NT}-L_{NL})^{A_2}}+H_N \tag{2.10}$$

A top view shape can be expressed in Eq. (2.11), as shown in Fig. 2.8-(b) [32].

$$Y_T(x) = \begin{cases} \dfrac{0.5W_T}{L_{NT}^{A_1+A_2}} x^{A_1}(2L_{NT} - x)^{A_2} & (0 \le x \le L_{NT}) \\ 0.5W_T & (L_{NT} \le x \le L_T) \end{cases} \tag{2.11}$$

After defining the side and top view shapes, all cross-sections have to be defined along the length of a train from a front end to a rear end as

$$Z_{FU}(x,y) = \frac{Z_{SU}(x) - H_N}{Y_T(x)^{A_1+A_2}}[y + Y_T(x)]^{A_1} \times \{2Y_T(x) - [y + Y_T(x)]\}^{A_2} + H_N \qquad (0 \le y \le Y_T(x)) \tag{2.12}$$

$$Z_{FL}(x,y) = \frac{Z_{SL}(x) - H_N}{Y_T(x)^{A_1+A_2}}[y + Y_T(x)]^{A_1} \times \{2Y_T(x) - [y + Y_T(x)]\}^{A_2} + H_N \qquad (0 \le z \le H_N) \tag{2.13}$$

In Eqs. (2.12-13), $Z_{FU}(x, y)$ and $Z_{FL}(x, y)$ represent the upper and lower cross-section shapes, respectively [32]. The $Z_{SU}(x)$, $Z_{SL}(x)$ and $Y_T(x)$ are defined in Eqs. (2.7-11).

For side and top view shape, the design variables A_1 and A_2 are fixed for a given shape. However, the cross-section shapes are varied along the length. Therefore, A_1 and A_2 are changed from circle-like shape to rectangular-like shape. For upper cross-section shape, the A_1 and A_2 have a same value as

$$A_1 = A_2 = A_S + (A_E - A_S)\left(\frac{x}{L}\right)^{P_U} \tag{2.14}$$

Where, A_S and A_E are corresponded with the front and rear cross-section shape respectively and the parameter P_U determines a speed of change from a front to a rear end [32]. The lower cross-section shape is done in a same way.

As the attached part, only a cockpit window is installed in this study. To represent a three-dimensional cockpit window shape as shown in Fig. 2.9, the height of a cockpit window are given as

$$Z_{CW}(x,y)=\frac{Z_{B,CW}(x)}{Y_{B,CW}(x)^{A_1+A_2}}[y+Y_{B,CW}(x)]^{A_1}[-y+Y_{B,CW}(x)]^{A_2} \tag{2.15}$$

where,

$$Y_{B,CW}(x)=\frac{0.5W_{CW}}{(0.5L_{CW})^{A_1+A_2}}(x-X_{CW})^{A_1}[L_{CW}-(x-X_{CW})]^{A_2} \tag{2.16}$$

$$Z_{B,CW}(x)=\frac{H_{CW}}{(0.5L_{CW})^{A_1+A_2}}(x-X_{CW})^{A_1}[L_{CW}-(x-X_{CW})]^{A_2} \tag{2.17}$$

Then, z-coordinates of a cockpit window are added to the z-coordinates of a train nose as

$$Z(x,y)=Z(x,y)+Z_{CW}(x,y) \tag{2.18}$$

To construct the constrained train nose model in Chap. 4, the optimized cross-sectional area distribution of a high-speed train nose is used as the constraint of the three-dimensional train nose. For this procedure, the cross-sectional area has to be calculated mathematically [32].

With the assumption of *H=L=1*, the area can be calculated by integration of parts.

$$Area = \int_0^L f(x)dx = \int_0^L x^{A_1}(2L-x)^{A_2}\,dx \tag{2.19}$$

Eq. (2.19) can be rewritten by a summation of each term as

$$\int_0^L x^{A_1}(2L-x)^{A_2}\,dx = \sum_{N=1}^{\infty} F_N \tag{2.20}$$

where,

$$F_1 = \frac{1}{A_1+1} L^{A_1+A_2+1} \tag{2.20-a}$$

$$F_2 = \frac{A_2}{(A_1+1)(A_1+2)} L^{A_1+A_2+1} \tag{2.20-b}$$

$$F_3 = \frac{A_2(A_2-1)}{(A_1+1)(A_1+2)(A_1+3)} L^{A_1+A_2+1} \tag{2.20-c}$$

$$\vdots$$

$$F_N = \frac{A_2(A_2-1)\cdots(A_2-N+2)}{(A_1+1)(A_1+2)\cdots(A_1+N)} L^{A_1+A_2+1} \tag{2.20-d}$$

As the order of F_N increases, the result becomes more accurate. In this research, the 16^{th}-order of F_N is used and the error is less than 0.01 %. The detail of the integration of parts is described in Ref. [32].

From the procedure for calculating the cross-sectional area, the cross-sectional area at x-position is a function of f as

$$Area = f(A_1, A_2, L, H) \tag{2.21}$$

Therefore the variables can be determined inversely for the given cross-sectional area [32]. If variables A_1, A_2 and L are fixed, the height is an inverse function of f as

$$H = f^{-1}(Area, A_1, A_2, L) \tag{2.22}$$

Other variables can also be calculated inversely in a similar way. Using this procedure, the three-dimensional nose shape has to be produced and modified keeping the optimized cross-sectional area distribution

2.3 Design Optimization Method

2.3.1 Design of Experiments (DOE) – Maximin Latin Hypercube Sampling

Latin Hypercube Sampling (LHS) is the first type of design proposed specifically for computer experiments [42]. LHS is a matrix of n rows and k columns where n is the number of levels being examined and k is the number of design variables. Each of the k columns contains the levels 1, 2, ..., n, randomly permuted, and the k columns are matched at random to form the LHS. The LHS offer flexible sample sizes while ensuring stratified sampling. The design can have relatively small variance when measuring output variance [43]. It is known to scatter the experimental points over the design space without any superposition [44].

The Maximin Latin Hypercube Sampling (Maximin LHS) is a type of improved LHS, which is originally proposed by Johnson, Moore and Ylvisaker [44,45]. This sampling method maximizes the minimum distance between arbitrary two sampling points for regular exploration of the design space. Fig. 2.10 shows an example of the Maximin LHS for two variables and nine sampling points. In the present study, the twenty five sampling points by the Maximin LHS method are extracted for the construction of the aritificial neural network models for five design variables of the unconstrained optimization problem and for four design variables of the constrained optimization problem.

2.3.2 Design Space Approximation - Artificial Neural Network

Neural Network (NN) was created based on the ideas of how human nervous system transfers and handles the information. It understands the behaviors of output variables by input variables and defines the relationship between the input variables and the output variables in a mathematical form. NN has a good advantage in representing the nonlinear problems of the complex system [46-48]. In the NN method, data processing unit which is called "Neuron" assemble and judge from the existing state of things in the design optimization problem. Neuron adds external stimuli with multiplying weighting factors, then delivers the data to the next neuron by a transfer function. The set of the neurons, which uses same previous data, is defined as "Layer" and the whole Artificial Neural Network (ANN) is constructed by assembling the layers. Generally, three-layer artificial neural network is commonly used and it is comprised of an input layer, a hidden layer, and an output layer, as shown in Fig. 2.11.

In order to perform the efficient design optimization, NN models replaced the aerodynamic analysis in this study. The ANN is constructed for the approximation model because an ANN is known to represent various nonlinear phenomena well, as mentioned above [46]. The ANN model for the unconstrained problem is composed of the input layer with 5 neurons (5 design variables), the hidden layer with 8 neurons, and an output layer with 1 neuron (C_D). Next, The NN model for the constrained problem is composed of the input layer with 4 neurons (4 design variables), the hidden layer with 6 neurons, and an output layer with 1 neuron (C_D). The adjusted R^2 of the NN models in both problems were about 0.99. Therefore, the ANN models used in this study deemed to be well constructed.

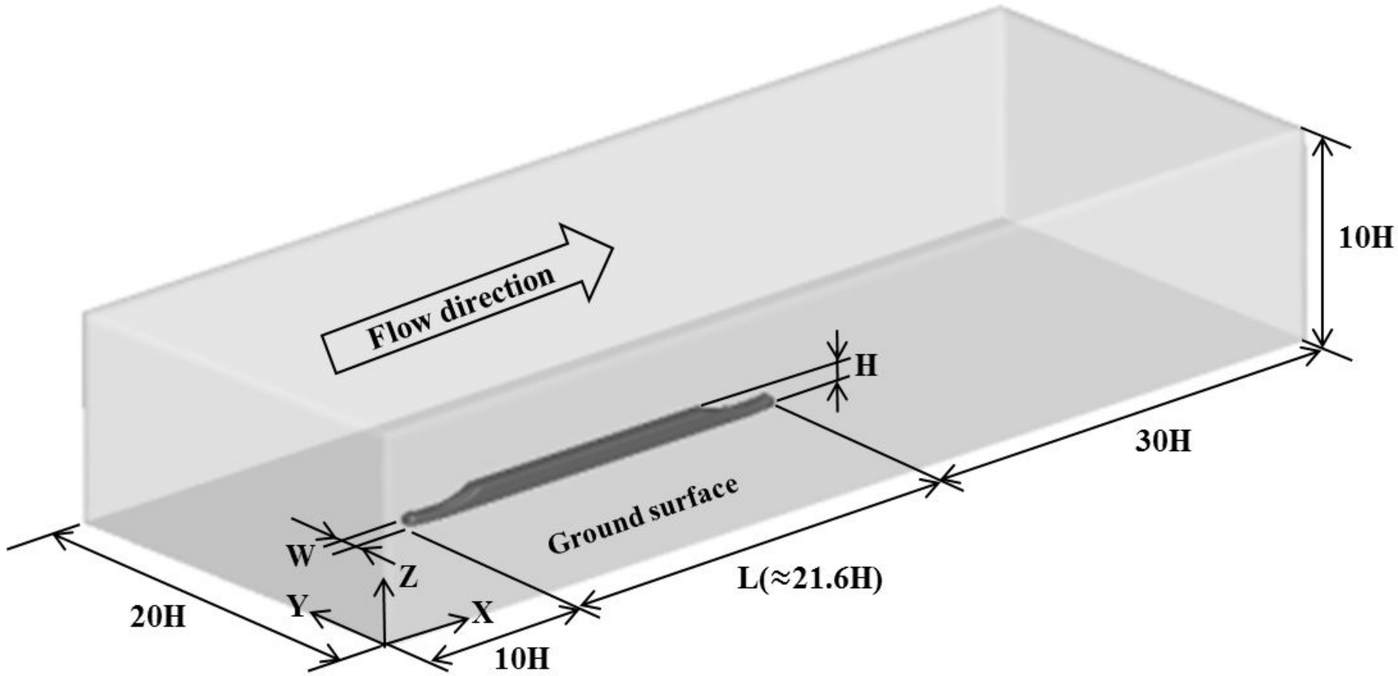

Fig. 2.1 Dimensions of the computational domain

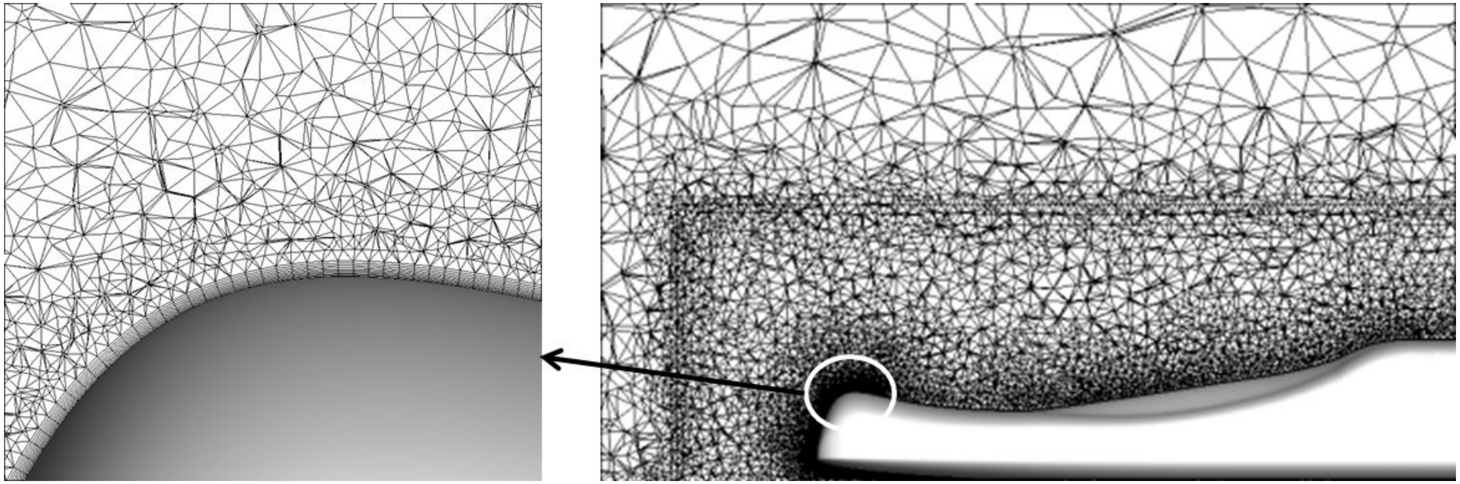

Fig. 2.2 The grid system at the symmetric center section around the first car nose of the train model

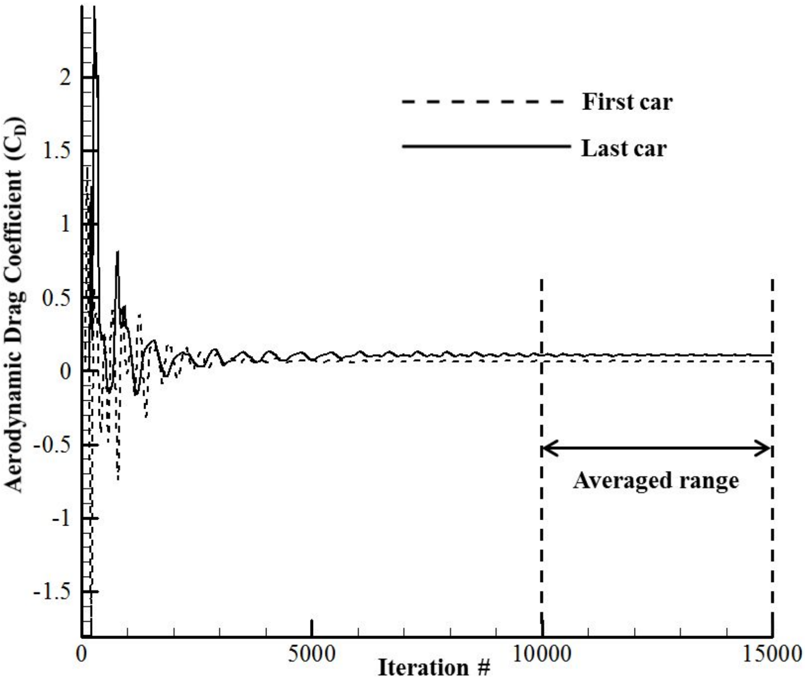

Fig. 2.3 C_D history of the base model during numerical simulation with V=500 km/h and stable range for calculating averaged C_D

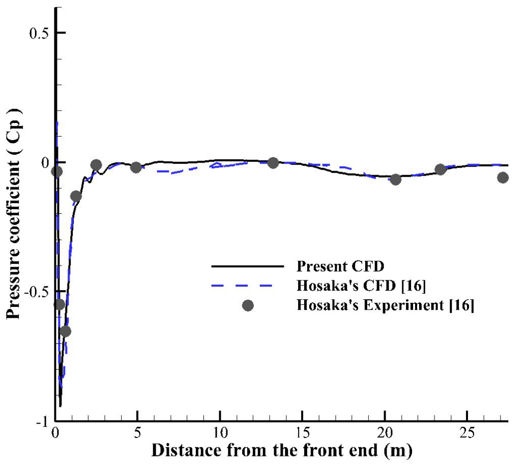

(a) On the surface of the first car

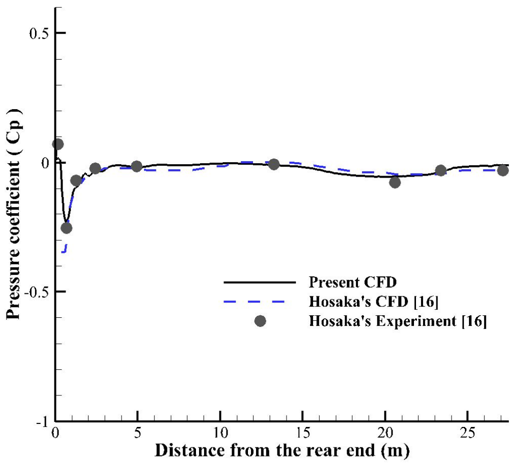

(b) On the surface of the last car

Fig. 2.4 Comparisons of surface pressures along the centerline between the present numerical results and the previous numerical and experimental data for MLX01, Japanese Maglev train under development [16]

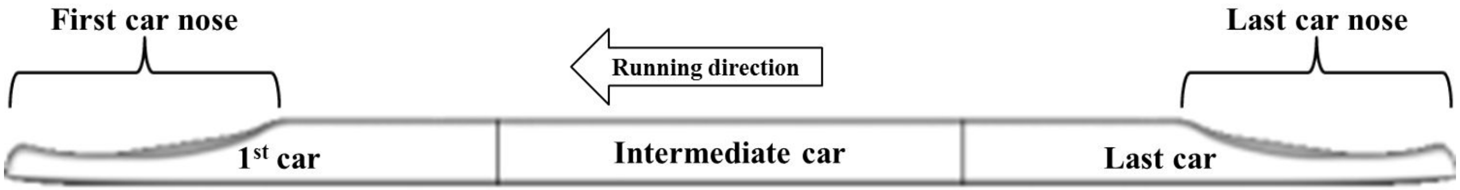

Fig. 2.5 A three-car streamlined model with no bogie wheel for a front-rear symmetric train model

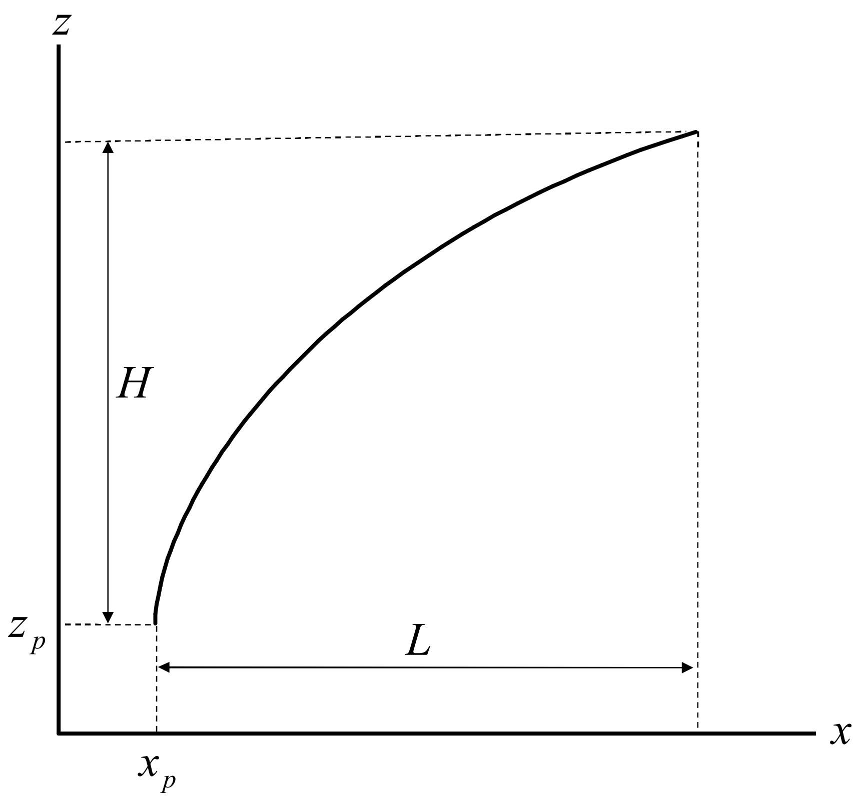

Fig. 2.6 Basic curve shape of the Vehicle Modeling Function [32]

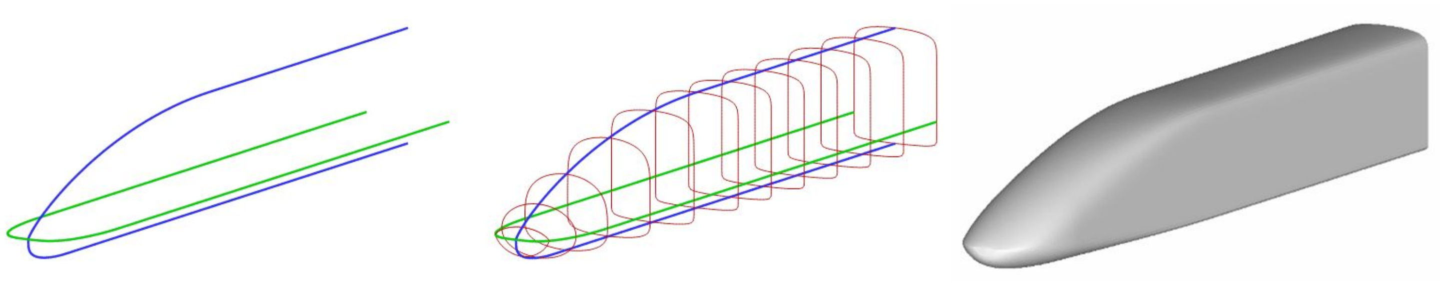

Fig. 2.7 The modeling process of a three-dimensional train body with the Vehicle Modeling Function [32,33,41]

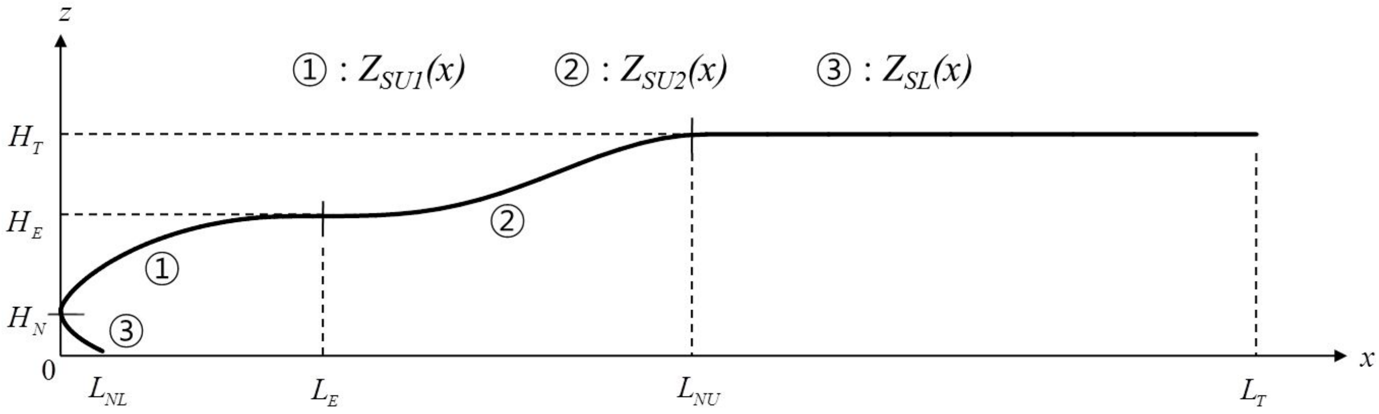

(a) Side View Shape of 2-Box Model

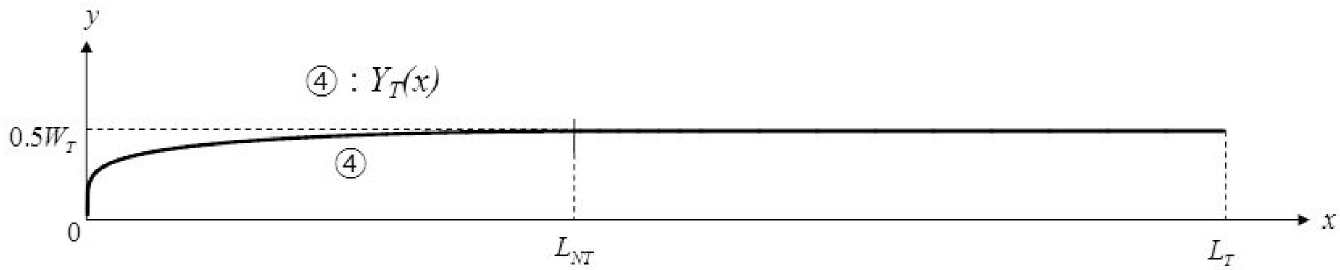

(b) Top View Shape

Fig. 2.8 Side and top view shapes of a train nose and corresponding functions [32,33]

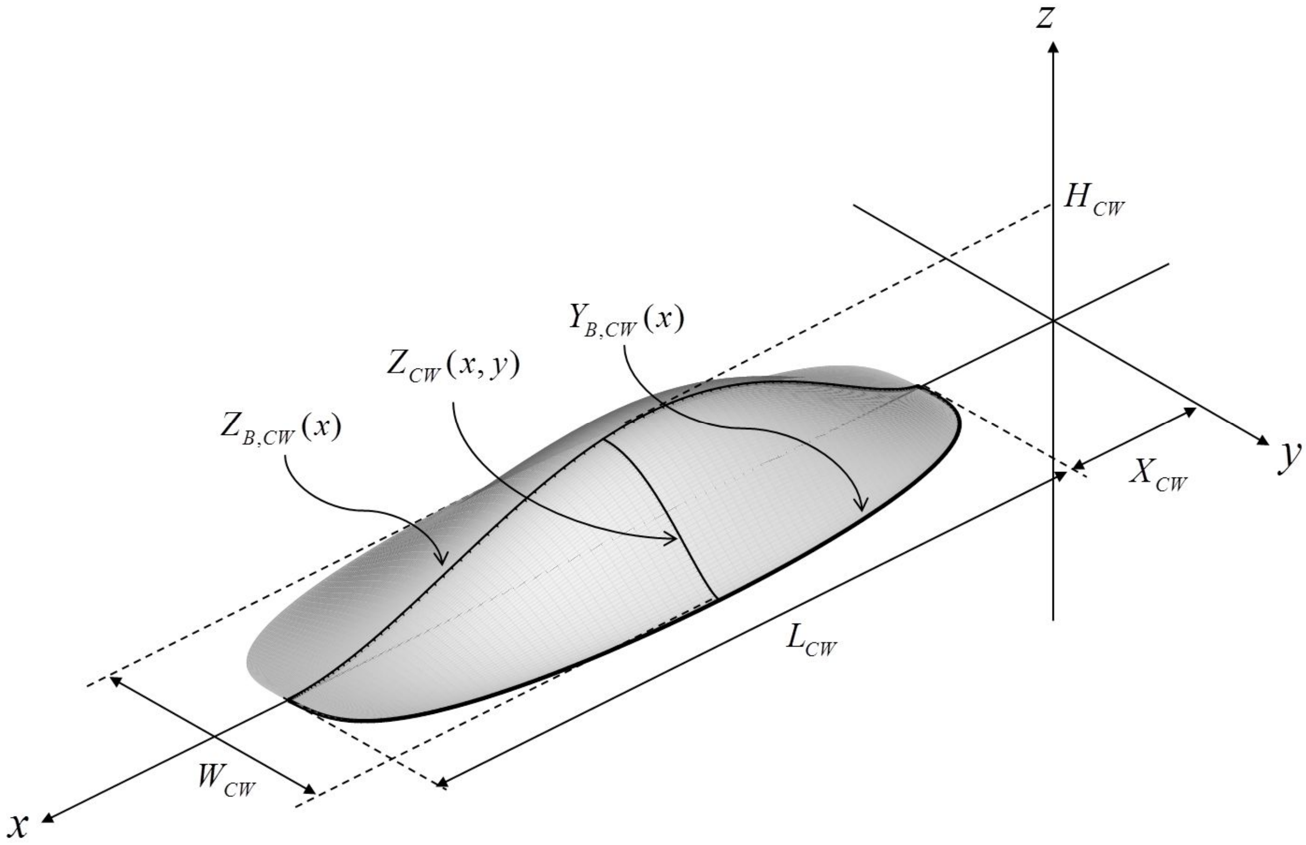

Fig. 2.9 3D shape of cockpit window [32,33]

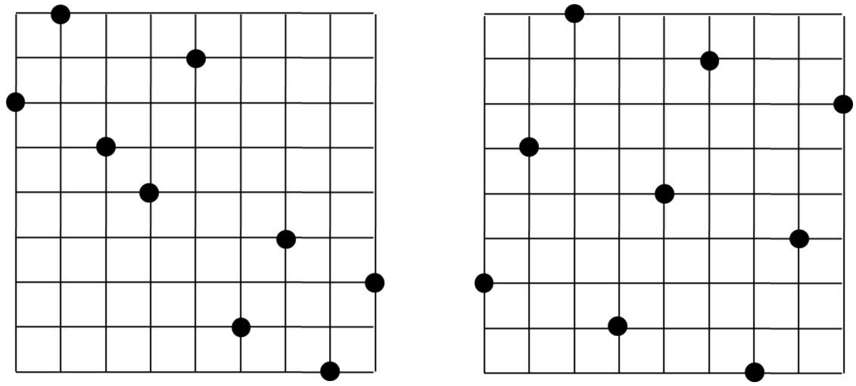

(a) Latin Hypercube Sampling (b) Maximin Latin Hypercube Sampling

Fig. 2.10 Space-filling design [44]

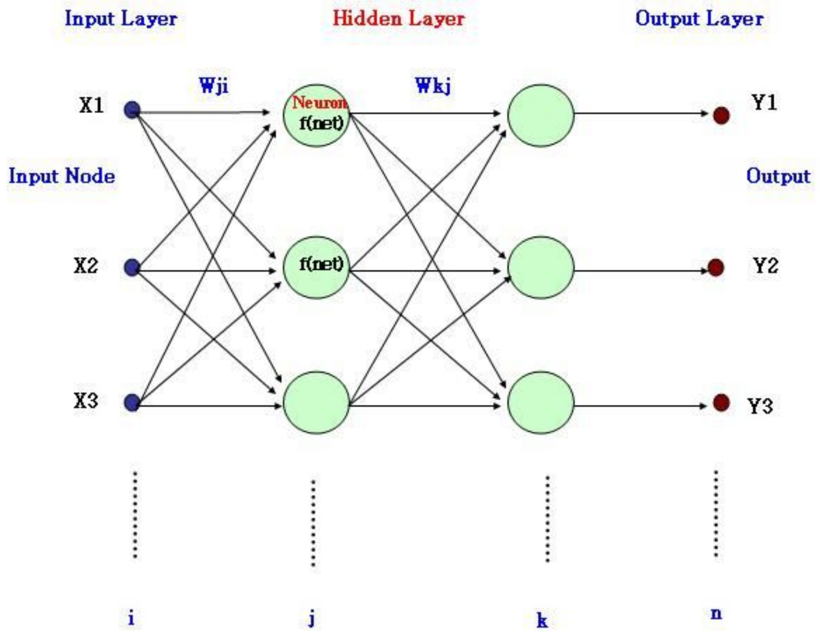

Fig. 2.11 Structures of an artificial neural network [46-48]

Chapter 3. Nose Optimization with Unconstrained Train Model

3.1 Design Problem Formulation

In these unconstrained optimizations, the objective is the reduction of the total aerodynamic drag of the entire train. The optimizations are conducted for two cases below.

1. Case I : The optimization is conducted to reduce the total aerodynamic drag of the entire symmetric train. The total aerodynamic drag of the entire train is calculated from the sum of all the aerodynamic drag of the first car, of the intermediate car, and of the last car.

   Determine 3-D shape of train nose

   Minimize $C_{D\ \text{entire train}}\ (= C_{D\ \text{first car}} + C_{D\ \text{intermediate car}} + C_{D\ \text{last car}})$ (3.1)

2. Case II : The optimization is performed to minimize the aerodynamic drag of only the first car by the previous method for the reduction of the design time.

   Determine 3-D shape of train nose

   Minimize $C_{D\ \text{first car}}$ (3.2)

With the maximum width and the maximum height fixed, the train shape is constructed by the Vehicle Modeling Function. The three-dimensional nose shape can vary without any constraint in these unconstrained optimization problems. However, the first car nose and the last car nose are still identical and always take on the same shape because the train used for the analysis is a front-rear symmetric train.

As shown in Fig. 3.1, a nose shape from a side view is composed of a upper nose curve and a lower nose curve. The upper nose curve is formed with the first upper nose curve and the second upper nose curve for a two box train model. A base model and a design space are determined maintaining train's own shape characteristics and considering the maximum dimension of the train. Thirteen shape parameters are selected because they are expected to have more effects on the aerodynamic drag of a front-rear symmetric train. They are the contact point, the end point and the curvature. Fig. 3.1 shows shape parameters from a side view. First, L_{UN} is the length of the upper nose curve while L_{LN} is that of the lower nose curve. H_N is the height of the point where the upper nose curve and the lower nose curve meet. X_{IN} and Z_{IN} are the coordinate of the point where the first upper nose curve and the second upper nose curve of the 2-box train model are connected. A_{U1} is the factor that controls the curvature of the first upper nose curve, whereas A_{U2} is the factor that controls the curvature of the second upper nose curve. A_L controls the curvature of the lower nose. Fig. 3.2 shows A_T which controls the curvature of the nose curve from a top view. A_{FU} and A_{FL} control the curvature of the upper corner and that of the lower corner on the fore cross section shape from a front view respectively, as shown in Fig. 3.3. P_U is the variable that determines the speed of the change along the nose from the circular-like end shape to the rectangular-like shape of the part where the nose ends. H_{CW} is the height of the cockpit window, as shown in Fig. 3.4.

3.2 Different Aerodynamic Effects of One Same Nose on the First Car and on the Last Car

The flow characteristics around the base train model are shown in Fig. 3.5. The flow goes along the train surface toward the rear without any complex region. In the vicinity of the last car, the flow passing the train tends to go in the lower direction due to train's shape feature. Then, most of the flow from all sides is mixed and some parts of them formed helical vortices [5]. The aerodynamic drag of the last car is almost same to that of the first car.

For the efficient design optimization, it is necessary to select a number of crucial design variables which have more effects on the total aerodynamic drag. Therefore, the sensitivity analyses are necessary. The sensitivity analyses for these shape parameters are progressed by calculating the variation rate of the aerodynamic drag from the lower bound to the upper bound, as shown in Table 3.1.

The length of the upper nose (L_{UN}) is most effective on the aerodynamic drag of the train. Additional five shape parameters but L_{UN} take more effects on the aerodynamic drag than the other shape parameters. They are the height of the point where the upper nose curve and the lower nose curve meet (H_N), the coordinate of the point where the first box and the second box of the 2-box train model are connected (X_{IN} and Z_{IN}), the factor that controls the curvature of the second upper nose curve (A_{U2}), and the curvature of the nose from a top view (A_T).

The upper nose length of all train shape for the optimization process is changed to 15m from 10m because the total aerodynamic drag is certainly reduced as the upper nose length is 15m. The upper nose length of the base model in the sensitivity analyses is also changed to 15 m and this edited base model is used for the base model of the optimization process. The other five shape parameters which take greater effects on the aerodynamic drag, H_N, X_{IN}, Z_{IN}, A_{U2}, A_T, are chosen for design variables of the optimization processes. Values of the base model and the ranges of the design variables are summarized in Table 3.2. Artificial Neural Network is constructed with twenty five experimental points extracted by Maxi-min Latin Hypercube Sampling method. The adjusted R^2 of the meta-model was about 0.99. Therefore the ANN deemed to be well constructed. The Broyden-Fletcher-Goldfarb-Shanno (BFGS) algorithm, a gradient-based method, is used as the optimization algorithm because the BFGS is appropriate for the unconstrained problem [49].

3.3 Comparison of the Optimized Model for Entire Train and the Previously Optimized Model

Table 3.3 shows comparison of the base model in the sensitivity analysis, the edited base model, and the optimized shape in case I. When comparing the base model and the edited base model, the aerodynamic drag of the first car is decreased by 8% and that of the entire train is done by 13%. When comparing the base model and the optimized shape in case I, the aerodynamic drag of the first car is decreased by 11% and that of the entire train is done by 18%. The aerodynamic drag of the last car is reduced comparatively as the upper nose length is increased to 15m. When comparing streamlines of the base model and the edited base model, the helical vortices are weakened behind the last car as the upper nose length becomes longer.

Fig. 3.6 shows comparison of the aerodynamic drag coefficients of the first car and those of the entire train for the edited base model and both optimized shapes respectively. The total aerodynamic drag of the entire train with the optimized shape in case I is reduced by 5.8% when compared to the edited base model, whereas the aerodynamic drag of the first car is reduced by only 2.8%. The aerodynamic drag of the last car is reduced more than that of the first car through the optimization considering the entire train. On the other hand, the total aerodynamic drag of the entire train with the optimized shape in case II is changed little, although the aerodynamic drag of the first car is reduced by 4.0% when compared to the edited base model.

Each variation of the pressure drag and the viscous drag are compared respectively between the base model and the optimized shape in case I to investigate the aerodynamic drag variation by the optimized shape more precisely, as shown in Table 3.4. For the first car, the pressure drag is reduced by 47.5% while the viscous drag is reduced by 4.9%. For the last car, the pressure drag is reduced by 70%, whereas the viscous drag is reduced by 11.1%. The pressure drag is reduced considerably by the optimized shape both for the first car and for the last car. It can be said that the shape deformation by the optimized shape is effective for reducing the aerodynamic drag.

It shows the importance of $C_{D\ \text{last car}}$ from a view of the total aerodynamic drag reduction even though $C_{D\ \text{last car}}$ is smaller than $C_{D\ \text{first car}}$. It can be said that shape optimization with consideration of both the first car nose and the last car nose (case I) is necessary to reduce the aerodynamic drag of the train model effectively.

The side view and the top view of the edited base model and the optimized shape in case I are compared in Fig. 3.7. From a two-dimensional side view, the optimized shape shows a lower end height of the nose tip and has the more convex cockpit window. Moreover, the curvature of the corner curves from the top view is smaller for the optimized shape case I. Therefore, the optimized shape in case I is vertically wider and horizontally thinner than the edited base model. All design variables of the optimized shape in case I are laid on the boundary of the design space.

The three-dimensional shapes of the edited base model and the optimized shape in case I are shown in Fig. 3.8. The edited base model seems like Fastech 360s, which is developing Japanese ultra-high-speed train [20]. It is a vessel-shaped train. The nose of the edited base model starts from a curve and its tip is a little blunt. On the other hand, the optimized shape in case I looks like a bird's beak and a tip of a fighter. The nose tip is very sharp and starts from a point toward the rectangle-type train body. The nose of the optimized shape points in a lower direction and has a long vertical end shape.

Streamlines behind the last car from two-dimensional side view are compared between the base model and the optimized shape in case I, as shown in Fig. 3.9, as most of the aerodynamic drag reduction occur at the last car. The flow along the last car of the edited base model is whirling near the tip of the last car nose. On the other hand, the flow along the optimized shape goes smoothly toward outside of the train.

To investigate the drag reduction caused by the optimized shape in case I more precisely, streamline patterns behind the last car from a three-dimensional isometric view are compared in Fig. 3.10. When compared with the edited base model, the streamlines behind the optimized shape in case I are likely to come into the center line due to the vertically wider nose shape. The up-wash flow from the underside causes the flow around the nose tip more complex and to be whirled. However, the optimized shape in case I prevents the flow from soaring and makes the flow smoothly go outward.

Fig. 3.11 and Fig. 3.12 show that the surface pressures of the optimized shape vary much less on both the upper surface and the lower surface when compared those of the edited base model. The lowest pressure of the optimized shape is also higher than that of the edited base model on both the upper surface and the lower surface. The total aerodynamic drag of the optimized shape is smaller than that of the edited base model because the greater base pressure reduces the aerodynamic drag of the vehicle [50,51].

Table 3.1 Aerodynamic drag variation between the lower bound, the base value, the upper bound of each design variable at Re# = 3.36×10^7

Shape parameter	Lower bound			Base model	Upper bound		
	Value	$\Delta C_{D,}$ First car	$\Delta C_{D,}$ Last car		Value	$\Delta C_{D,}$ First car	$\Delta C_{D,}$ Last car
L_{UN}	5	+14.8%	+109.7%	10	15	-8.3%	-26.5%
L_{LN}	1	+0.7%	+2.2%	2	5	-0.7%	-6.7%
H_N	0.5	-2.1%	-4.7%	1	1.5	+5.2%	+13.9%
X_{IN}	2.5	+0.8%	-11.9%	5	7.5	+11.5%	+107.6%
Z_{IN}	1.5	+2.2%	+20.2%	2	2.5	-0.1%	-12.9%
A_{U1}	0.4	+0.3%	+3.7%	0.7	1	+0.1%	-1.5%
A_{U2}	3	-0.5%	-8.1%	4.5	6	+0.4%	+8.2%
A_L	0.4	-0.5%	+0.3%	0.7	1	+0.5%	+1.8%
A_T	0.01	+13.8%	+41.2%	0.505	1	-2.3%	-5.5%
A_{FU}	0.01	+3.5%	+4.9%	0.505	1	-0.5%	-7.4%
P_U	0.5	+0.4%	+6.4%	1.25	2	-0.4%	-5.3%
A_{FL}	0.01	+1.6%	+5.7%	0.505	1	-0.7%	-1.9%
H_{CW}	0.25	+0.1%	+6.5%	0.45	0.65	-0.1%	-2.5%

Table 3.2 The ranges of the design variables

	Lower bound	Base model	Upper bound
H_N	0.5	1.0	1.5
X_{IN}	5.0	7.5	10
Z_{IN}	1.5	2.0	2.5
A_{U2}	3.0	4.5	6.0
A_T	0.01	0.505	1.0

Table 3.3 Aerodynamic drag variation among the base model, the edited base model, and the optimized model in case I at Re# = 3.36×10^7

Base model		Edited base model	Optimized model in case I
0.064	$\Delta C_{D\ \text{first car}}$	-8%	-11%
0.167	$\Delta C_{D\ \text{entire train}}$	-13%	-18%

Table 3.4 Pressure drag variation and viscous drag variation of the optimized model in case I when comparing with the edited base model

	First car	Last car
Pressure drag variation rate	-47.5%	-70.0%
Viscous drag variation rate	-4.9%	-11.1%

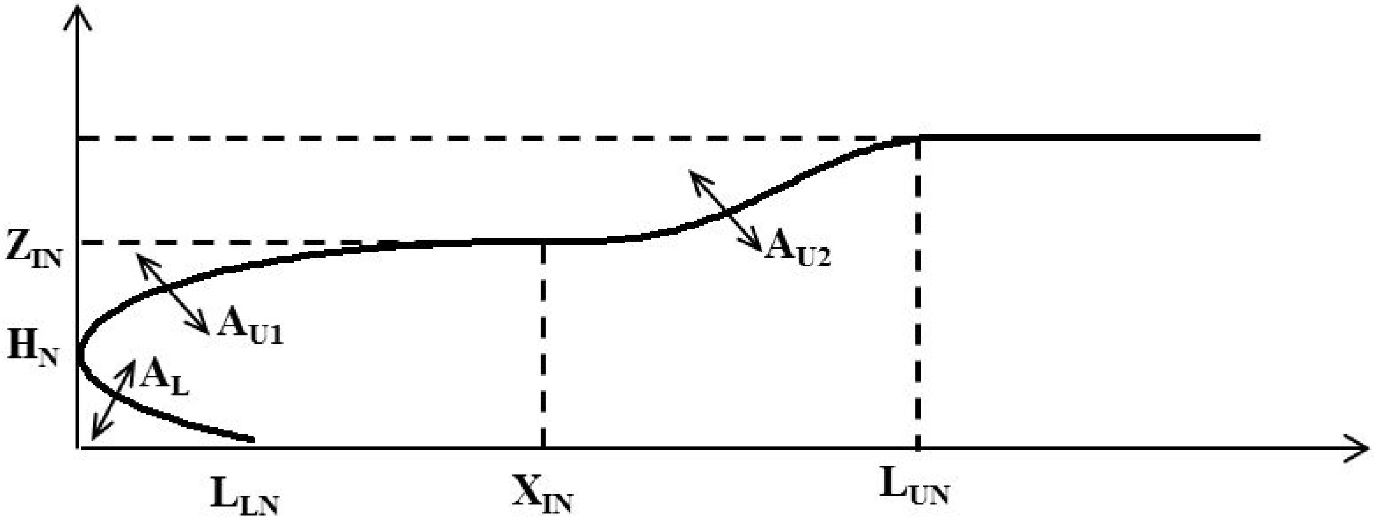

Fig. 3.1 Shape parameters with 2D side view

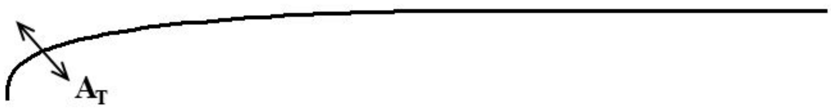

Fig. 3.2 Shape parameter with 2D top view

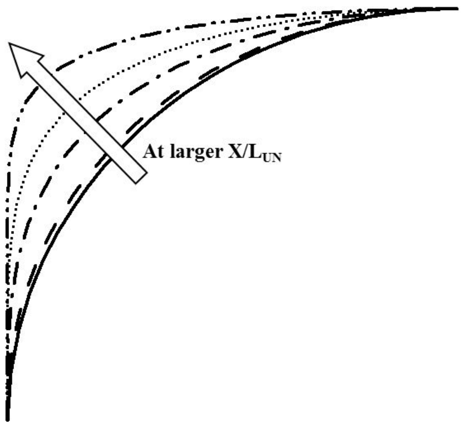

Fig. 3.3 Shape parameters with 2D front view

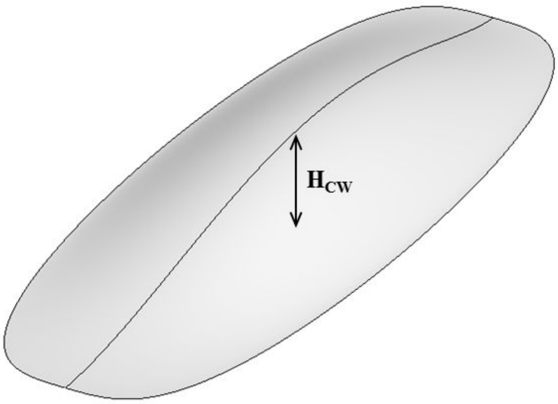

Fig. 3.4 Shape parameter of the cockpit window

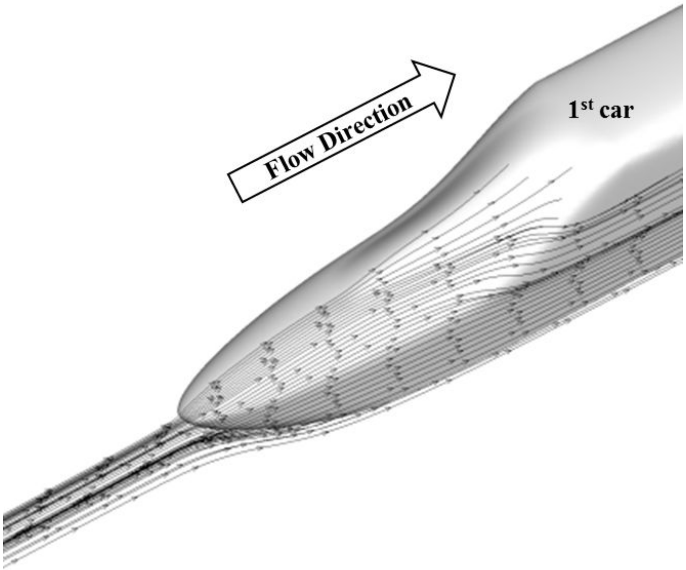

(a) Around the first car

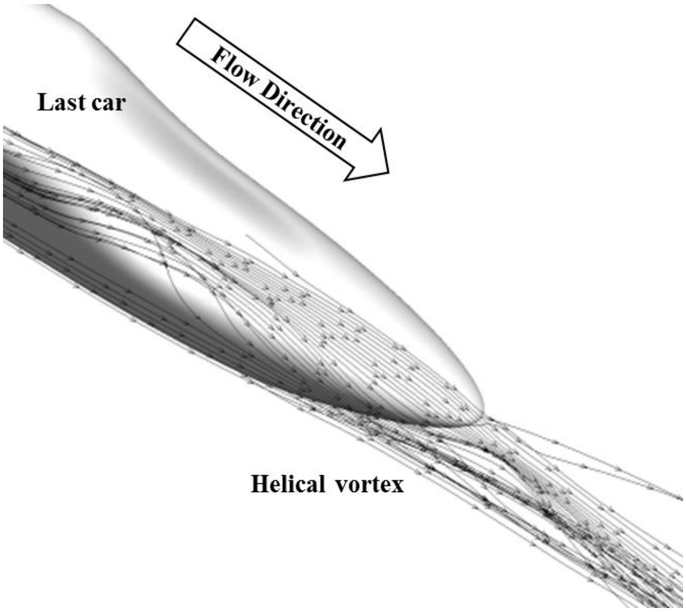

(b) Around the last car

Fig. 3.5 Numerically computed streamlines around the 3-car base model (L_{UN} = 10m) at V=500 km/h (at Re# = 3.36×10^7)

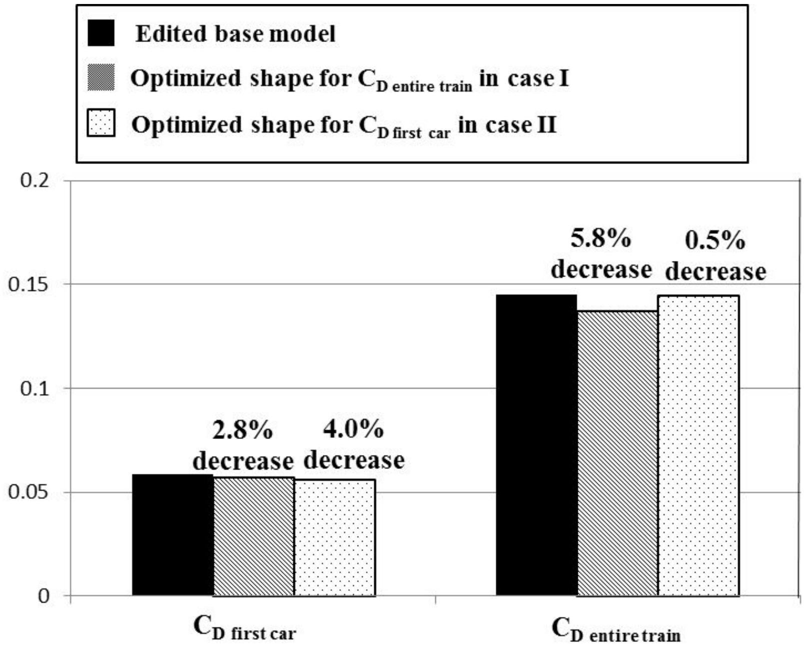

Fig. 3.6 Comparisons of drag coefficients between base model and the optimized shapes at V=500 km/h

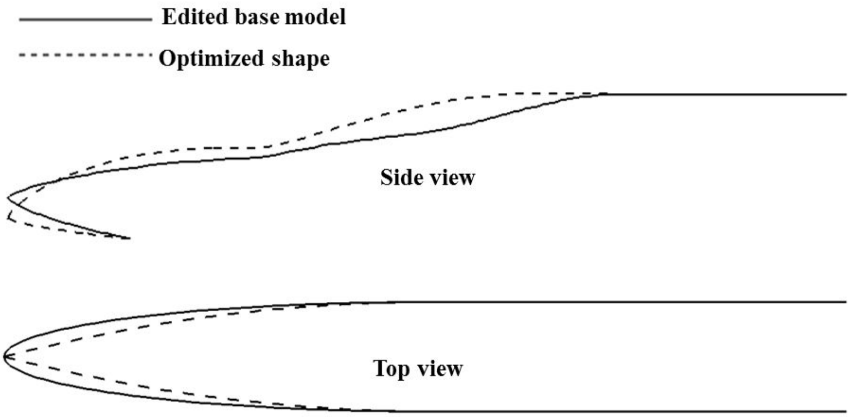

Fig. 3.7 Comparison of model forms between of the base model and of the optimized shape for $C_{D\ \text{entire train}}$ in case I from a 2D view

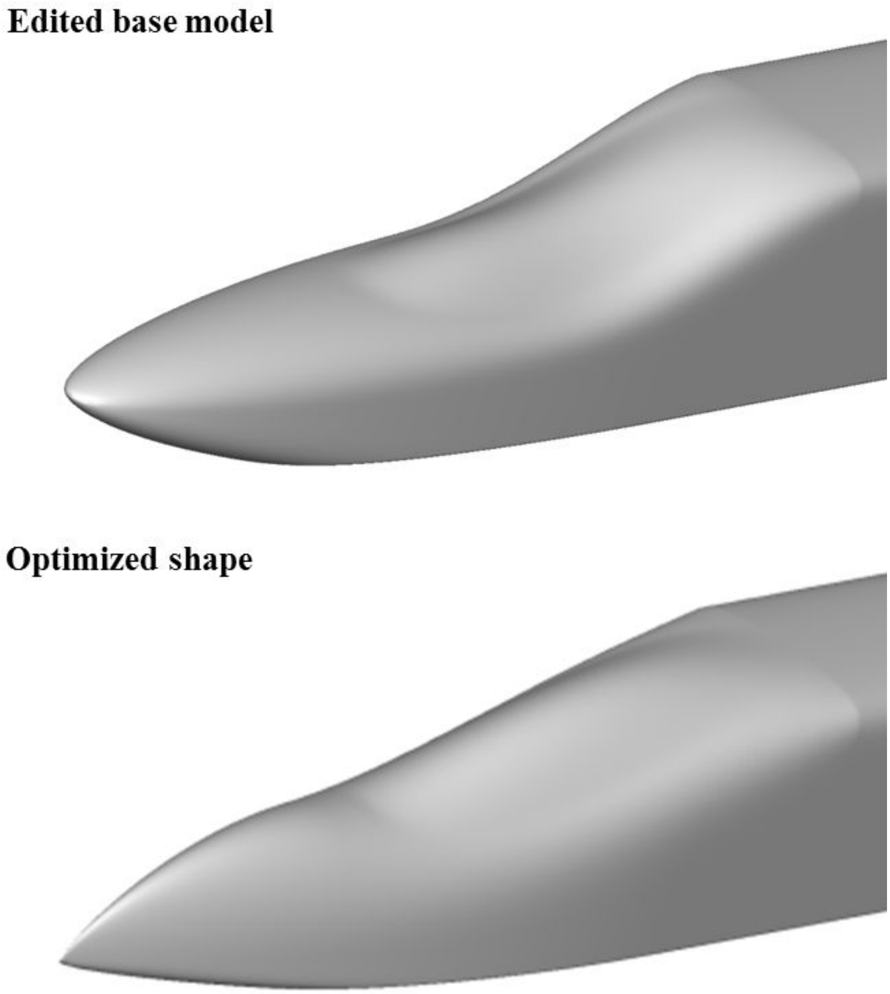

Fig. 3.8 Comparison of model forms between of the base model and of the optimized shape for $C_{D\ \mathrm{entire\ train}}$ in case I

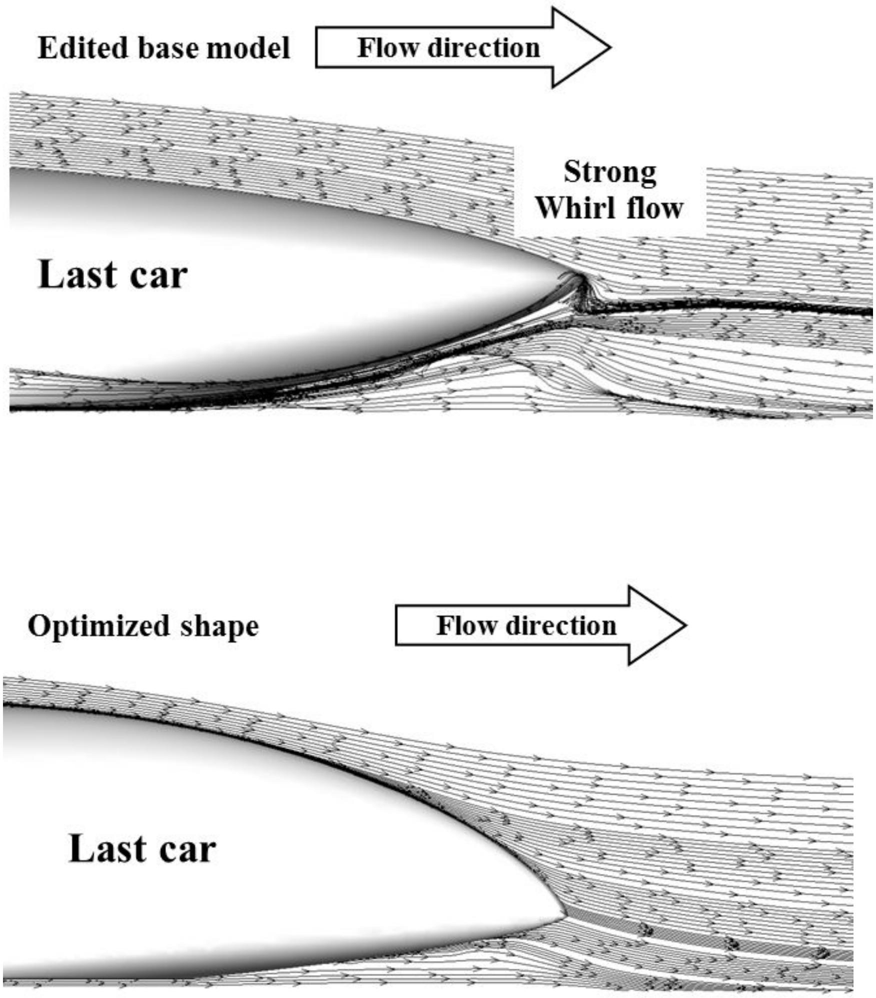

Fig. 3.9 Comparison of streamline patterns behind the last car with the two-dimensional side view between the edited base model and the optimized shape for $C_{D\ entire\ train}$ in case I at Re# = 3.36×10^7

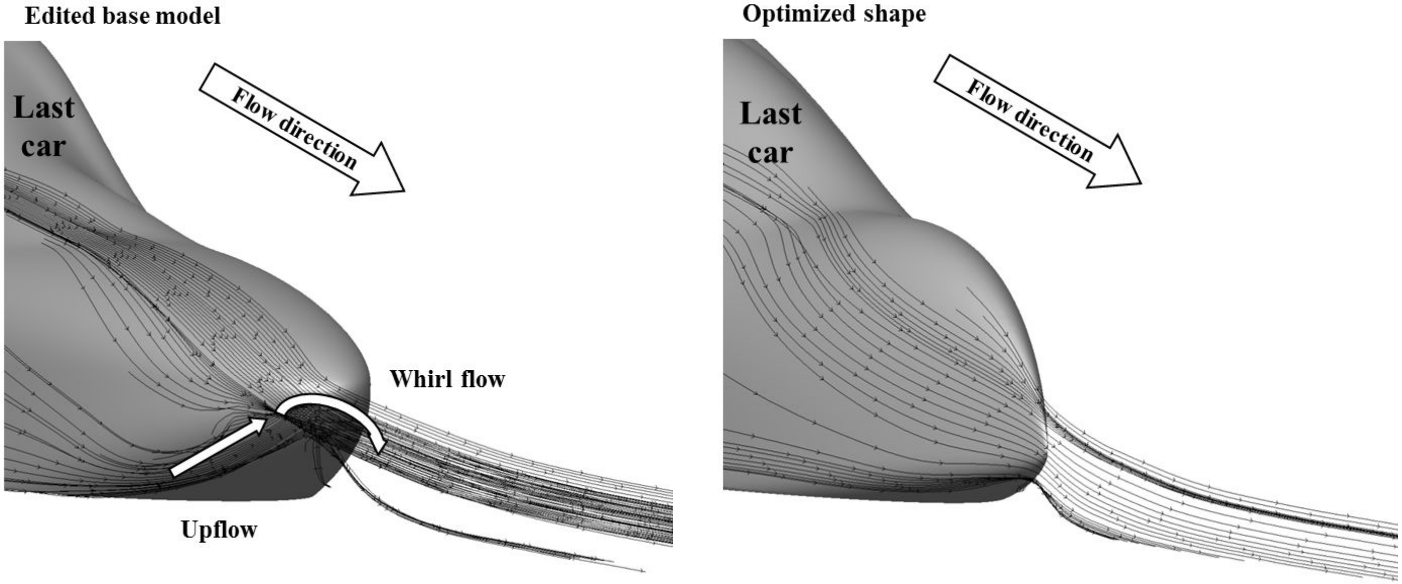

Fig. 3.10 Comparison of streamline patterns behind the last car between the edited base model and the optimized shape for $C_{D\ \mathrm{entire\ train}}$ in case I at Re# = 3.36×10^{7}

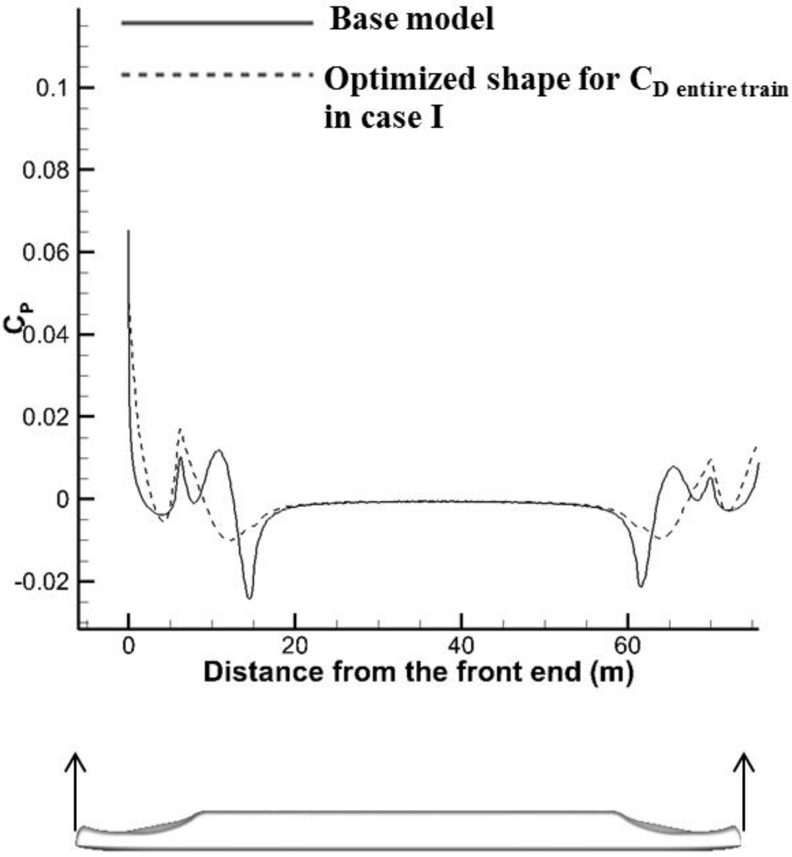

Fig. 3.11 Comparisons of pressure distributions on the train upper surface at the symmetric lateral centerline

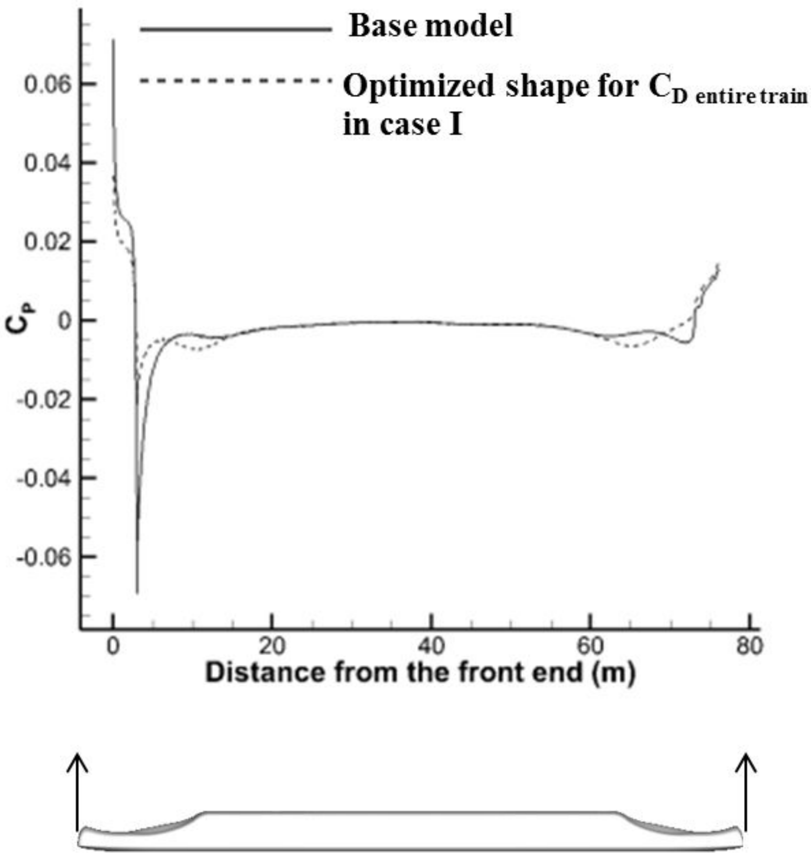

Fig. 3.12 Comparisons of pressure distributions on the train lower surface at the symmetric lateral centerline

Chapter 4. Nose Optimization with the Constrained Train Model

4.1 Design Problem Formulation

In these optimizations with the constraint of the modeling, the objective is the reduction of the total aerodynamic drag of the entire train and the micvro-pressure wave. The nose shape optimizations are conducted for the two cases.

1. Case I : The optimization is conducted to reduce the total aerodynamic drag of the entire symmetric train. The total aerodynamic drag of the entire train is calculated from the sum of all the aerodynamic drag of the first car, of the intermediate car, and of the last car.

   Determine 3-D shape of train nose

   Minimize $C_{D\ \text{entire train}}\ (= C_{D\ \text{first car}} + C_{D\ \text{intermediate car}} + C_{D\ \text{last car}})$ (4.1)

2. Case II : The optimization is performed to minimize the aerodynamic drag of only the first car by the previous method for the reduction of the design time.

   Determine 3-D shape of train nose

   Minimize $C_{D\ \text{first car}}$ (4.2)

The constraint of both optimization processes is the given optimized cross-sectional area distribution to maintain the minimum micro-pressure wave at the tunnel exit, as shown in Eq. (4.3). Each design range of each design variable is shown in Eq. (4.4)

Subject to :

Given optimized cross-sectional area distribution of the nose A(x) (4.3)

$$\begin{aligned} 0.05 \le A_T \le 0.15 \\ 0.32 \le H_N \le 0.72 \\ 0.5 \le P_U \le 2.0 \\ 0.25 \le H_{CW} \le 0.65 \end{aligned} \tag{4.4}$$

The Broyden-Fletcher-Goldfarb-Shanno (BFGS) algorithm, a gradient-based method, is used as the optimization algorithm because the given cross-sectional area distribution is the constraint of the three-dimensional shape modeling and the BFGS is appropriate for the unconstrained optimization problem [49].

The design optimization process starts from the one-dimensional cross-sectional area distribution optimized by Ku et al. as shown in Fig. 4.1 [2]. This distribution shape is obtained for the reduction of the micro-pressure wave. It has a blunt fore-end and the slope of the cross sectional area changes from a strong positive gradient to a negative gradient in the middle followed by a very steep increase in the rear of the nose. All the train shapes obtained in this study essentially satisfy the constraint of the optimized cross-sectional area distribution and show the minimum micro-pressure wave because the micro-pressure wave is affected mainly by the one-dimensional cross-sectional area distribution of the nose of the first car. The length of the cross sectional area distribution shape used in this study is 15m which is the longest length of the results by Ku et al. because longer noses induce the less aerodynamic load as the train speed increases [1,2].

In this optimization under the constraint of the optimized cross-sectional area distribution, the nose shape of the three-dimensional train body is produced by the VMF with the cross-sectional area distribution. Especially for the analysis of this front-rear symmetric train, the front nose and the rear nose are identical and always take on the same shape.

Four design variables are selected in variables which control the three-dimensional train shape because they are expected to have more effects on the aerodynamic drag of a high-speed train [32,33]. Because other design variables shown in Chap. 3 are changed little due to the constraint of the optimized cross-sectional area distribution, they cannot be used in this optimization with the constrained train model. The design variables, A_T, H_N, P_U, and H_{CW} are related to the bluntness of the top view corner shape, the fore/aft end height of noses, the corner shape of the upper cross-section shape, and the height of the cockpit window respectively. The design spaces for four design variables are very limited because the cross-sectional area distribution is the constraint of the optimization process. They are decided under the limit of not breaking the constraint and the three-dimensional model. A base model is selected of three-dimensional models based on the given one-dimensional cross-sectional area distribution considering the design space. Values of the base model and the ranges of the design variables are summarized in Table 4.1. Numerical simulations are conducted at both bounds of each design variable with other variables fixed. The results are compared with those of the base model to investigate the complex flow field around the first car and the last car.

After the base model analysis, the Maximin Latin Hypercube Sampling method is used to extract sampling points for the construction of the approximation model. 25 sampling points are selected for the four design variables. Numerical simulations at all sampling points are performed at the operating speed of 500 km/h. Next, an Artificial Neural Network (ANN) is constructed for the approximation model because an ANN is known to represent various nonlinear phenomena well [46]. The adjusted R^2 of the meta-model was about 0.99. Therefore the ANN deemed to be well constructed.

4.2 Different Aerodynamic Effects of One Same Nose on the First Car and on the Last Car

The flow characteristics around the base train model used in this study are shown in Fig. 4.2. A large stagnation point is created at the first car due to the blunt fore end shape of the front nose. The flow goes along the train surface toward the rear without any complex region such as a vortex. In the vicinity of the last car, the flow passing the train tends to go in the upper direction due to the strong up-wash flow from the underside of the train. Then, most of the flow from all sides is mixed and resembles a helical vortex [5]. The aerodynamic drag of the last car is comparatively large due to this complex flow region right behind the train.

Fig. 4.3~14 show the shape variations and the aerodynamic characteristics of the train at the lower bound, the base point, and the upper bound of each design variable. The aerodynamic drag and the pressure contour of the first car and the last car are compared respectively. As one design variable varies, the three-dimensional shape is changed not at one location but at two or more locations due to the constraint of the optimized cross-sectional area distribution.

Design variable A_T manages the bluntness of the nose shapes by changing the curvature of the nose curve from a top view as shown in Fig. 4.3. The bluntness of the nose shape from the top view decreases as A_T increases from the lower bound to the upper bound. Therefore, the train's fore/aft end looks horizontally wider at the lower bound of A_T. It looks vertically wider at its upper bound, however, due to the constraint. The aerodynamic drag of the first car at the lower bound changes only slightly when compared to the base model. However, the aerodynamic drag of the first car at the upper bound increases considerably because the vertically wider shape of the fore end induces larger vortices owing to the feature of the shape, as shown in Fig. 4.4. On the other hand, there are large variations of the aerodynamic drag of the last car between the lower bound and the upper bound. The aerodynamic drag of the last car at the lower bound is reduced by about 15.2 % when compared with the base model, whereas it is increased by about 23.3 % at the upper bound. The vertically wider shape of the aft end at the last car causes a very wide lower pressure region (the whiter area), as shown in Fig. 4.5 and this zone brings about a significant amount of the aerodynamic drag.

Design variable H_N controls the end height of the noses. As the height increases, the shapes of the noses rise in the upper direction as shown in Fig.4.6. In the case of the first car, the aerodynamic drag increases slightly both at the lower bound and at the upper bound. The difference is not great. However, H_N has a greater effect on the aerodynamic drag of the last car. As H_N increases, the aerodynamic drag also increases because the increase of the aft end height induces a more powerful up-wash flow from the underside and the strong vortices as shown in Fig.4.8.

Design variable P_U controls the upper cross-section shape. It is the variable that determines the speed of the change along the nose from the circular-like end shape to the rectangular-like shape of the part where the nose ends. The change speed is faster at the lower bound whereas it is slower at the upper bound. Therefore, both shoulder parts take on a more circular shape in the middle of the nose as P_U changes from the lower bound to the upper bound, as shown in Fig. 4.9. The height of the center part rather increases due to the optimized cross-sectional area distribution. There is little change in the aerodynamic drag of the first car as P_U changes, as presented in Fig. 4.10. In the case of the last car, there is a slight increase in the aerodynamic drag as P_U changes from the upper bound toward the lower bound, as shown in Fig. 4.11. At the lower bound of P_U, the more rectangular shape makes the flow easy to separate [52]. Lower pressure regions behind the train which cause an increase of the aerodynamic drag are reduced at the upper bound when compared to the base model and the lower bound model.

Design variable H_{CW} controls the height of the cockpit window as shown in Fig. 4.12. A greater height of the cockpit window reduces the thickness of the train body near the cockpit due to the constraint of the optimized cross sectional area distribution. In the two cases of the first car and the last car, there is somewhat of a difference.

To summarize, there is a little change in the aerodynamic drag of the first car according to shape changes because of the large stagnation point caused by the very blunt fore end shape except in the case of the upper bound of design variable A_T. Of all design variables, A_T, the bluntness of the top view corner shape, is the factor that has the strongest effect on both the aerodynamic drag of the first car and that of the last car. The aerodynamic drag characteristics due to one same nose shape vary depending on whether it is located at the first car or at the last car.

4.3 Comparison of the Optimized Model for Entire Train and the Previously Optimized Model

After the two optimization processes for the entire train and for only the first car are completed, the same optimized nose shape is applied to the front nose and the rear nose. Then numerical computations are conducted for the two optimum nose shapes, as shown below, to obtain the aerodynamic drag.

1. The optimized shape for $C_{D\ \mathrm{entire\ train}}$ in case I
2. The optimized shape for $C_{D\ \mathrm{first\ car}}$ in case II

The aerodynamic drag forces for the base model and the two optimized shapes are summarized in Table 4.2. For all three models, the aerodynamic drag of the last car is the largest one in three cars of the train while that of the intermediate car is smallest. In addition, Fig. 4.15 shows comparison of the aerodynamic drag coefficients of the first car and those of the entire train for the base model and both optimized shapes respectively. The aerodynamic drag of the entire train with the optimized shape in case I is reduced by 15.3% when compared to the base model, and by 23.0% when compared to the optimized shape in case II separately. Although the aerodynamic drag of the first car is increased slightly by about 2.8% with the optimized shape in case I when compared to the base model, the total aerodynamic drag is considerably reduced due to the large reduction of the aerodynamic drag in the last car. On the other hand, for the optimized shape in case II, there is little difference in the aerodynamic drag of the first car when compared to the base model due to the blunt fore end shape of the first car. Although the optimization is conducted, the total aerodynamic drag of the train in case II is increased by about

9.9 % when compared to the base model.

Each variation of the pressure drag and the viscous drag are compared respectively between the base model and the optimized shape in case I to investigate the aerodynamic drag variation by the optimized shape more precisely, as shown in Table 4.3. For the first car, the pressure drag is increased by 14% while the viscous drag is reduced by 2.3%. For the last car, the pressure drag is reduced by 29.3%, whereas the viscous drag is reduced by 3.4%. The pressure drag is reduced considerably by the optimized shape for the last car. It can be said that the shape deformation by the optimized shape is effective for reducing the aerodynamic drag.

It shows the importance of $C_{D\ last\ car}$ in the total aerodynamic drag. It can be said that shape optimization with consideration of both front nose and the rear nose (case I) is necessary to reduce the aerodynamic drag of the train model effectively.

The optimized shape in case I is compared with the base model as shown in Fig. 4.16. From a two-dimensional side view, it shows a lower end height of the noses and a lower height of the cockpit window. Moreover, the curvature of its curve at the corners from the top view decreases. Therefore, the nose of the train body points in a lower direction and has a wide horizontal end shape. All design variables of the optimized shape in case I are laid on the boundary of the design space because the design space are very limited due to the constraint of the optimization process, the given cross-sectional area distribution.

Streamlines behind the last car from two-dimensional side view are compared between the base model and the optimized shape in case I, as shown in

Fig. 4.17, as most of the aerodynamic drag reduction occurs at the last car. The flow around the base model generates a larger vortex near the top due to the strong up-wash flow from the underside of the train. Greater vortices and a powerful up-wash flow cause the flow which passes the base model to rise more. On the other hand, the optimized shape in case I weakens the up-wash flow. Therefore, the vortices also become smaller and the flow which passes the optimized model tends to go upward less.

To investigate the drag reduction caused by the optimized shape in case I more precisely, streamline patterns behind the last car from a three-dimensional isometric view are compared in Figs. 4.18~21. The streamlines are divided into those from the underside, those from the upper side, those from the middle side, and those from the shoulder side. In the case of the base model, a strong up-wash flow moves out from underside of the last car as shown in Fig. 4.18. The flow soaring up makes the vortices stronger for the base model. Therefore, the flow rises higher and pulls the train backward more. However, the optimized shape in case I forces the up-wash flow to become weaker and induces weaker vortices. On the other hand, the flow from the upper side is affected by the powerful up-wash flow from the underside for the base model, as shown in Fig. 4.19. Therefore, the flow from the upper side tends to go higher like the flow from the underside. However, the flow from the upper side of the optimized shape in case I is not affected much by the weak up-wash flow. The flows from the middle side and from the shoulder side of the base model easily penetrate into the area directly behind the train, as shown in Figs. 4.20~21. Therefore, some of these streamlines are mixed with those from other directions and thus made strong vortices. On the other hand, the flows from the middle side and from the shoulder side of the optimized shape in case I do not make the flow complex and the flows move out backward smoothly. In summary, the low-rise body of the optimized shape prevents the up-wash flow from being strong and from creating a strong vortex. Furthermore the horizontally wider fore end shape disturbs the middle side flow and the shoulder side flow penetrating into the complex flow field behind the train. The aerodynamic drag of the last car of the optimized shape in case I is reduced owing to these flow patterns.

The pressure distributions along the symmetric lateral centerline surface of the train are shown in Fig. 4.22. The distributions for the upper surfaces and for the lower surfaces of the last car are magnified in each case. The pressure of the optimized shape in case I varies less than those of the base model on both surfaces. The lowest pressure on both surfaces of the optimized shape in case I is greater than those of the base model. The greater base pressure reduces the aerodynamic drag of the vehicle [50,51].

Generally, it is well known that optimized shapes of the front nose between for the aerodynamic drag and for the micro-pressure wave are conflicted [31]. Therefore, it is difficult to obtain an optimum nose shape with the objectives of reducing both the aerodynamic drag and the micro-pressure wave when considering only the front nose at the same time or in order. However, considering not the front nose only but both noses enables the shape optimization to achieve both objectives better.

4.4 Comparison of the Unconstrained Optimum Model and the Constrained Optimum Model

The unconstrained optimum train shape and the constrained optimum train shape are compared in terms of shape characteristics and the aerodynamic drag. From a side view, the end of the constrained optimum nose is much blunter than that of the unconstrained optimum nose, as shown in Fig. 4.23. On the contrary, the unconstrained optimum nose is more convex that the constrained optimum nose at the cockpit window part. From a top view, the end of the constrained optimum nose is also a lot blunter than that of the unconstrained optimum nose. The tip of the unconstrained optimum nose seems like a steep horn.

When the upper nose length is 15m, the aerodynamic drag of the first car is greater than that of the last car for the unconstrained optimum model. On the other hand, they are reversed for the constrained optimum model. The aerodynamic drag of the last car is much larger than that of the first car for the constrained optimum model. For both optimization processes, the reduction rate of the aerodynamic drag of the last car is still greater than that of the first car.

The very blunt shape of the constrained optimum nose induces strong vortices and more complex flow behind the last car of the train. It makes the aerodynamic drag of the last car increase considerably. Therefore, the total aerodynamic drag of the constrained optimum train is much greater than that of the unconstrained optimum train.

However, the train shape used in this study is the streamlined model without any bogie. Addition of bogies and gaps makes the difference of the total aerodynamic drag smaller between the unconstrained optimum train and the constrained optimum train. In the mountainous countries such as Korea and Japan, the reduction of the micro-pressure wave at the tunnel exit is as important as the reduction of the aerodynamic drag in the open field. Even though the total aerodynamic drag of the constrained optimum train is greater than the unconstrained optimum train, the micro-pressure wave still has to be considered for the nose shape design of the ultra-high-speed train.

Unlike the previous design optimization, the Vehicle Modeling Function let various three-dimensional shape modeling with or without the constraint of the modeling. The three dimensional modeling is very necessary because the wake area has to be simulated as accurately as possible for design optimization of the actual front-rear symmetric train. Therefore, it can be said that the Vehicle Modeling Function is a valuable tool in that it enables the three-dimensional modeling of the train body efficiently, leading to a successful three-dimensional shape optimization. It also can be concluded that considering both the first car nose and the last car nose at the same time is necessary for the effective optimization of the nose shape so as to minimize the total aerodynamic drag of the symmetric train.

Table 4.1 The ranges of the design variables [32]

	Lower bound	Base model	Upper bound
A_T	0.05	0.1	0.15
H_N	0.32	0.52	0.72
P_U	0.5	1.25	2.0
H_{CW}	0.25	0.45	0.65

Table 4.2 Aerodynamic drag coefficient of each car for the base model, the optimized shape in case I and the optimized shape in case II

Train model	$C_{D\ entire\ train}$	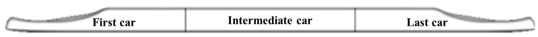		
		$C_{D\ first\ car}$	$C_{D\ intermediate\ car}$	$C_{D\ last\ car}$
Base model	0.2474	0.0641	0.0373	0.1460
Case I : Optimized shape for $C_{D\ entire\ train}$	0.2094	0.0658	0.0372	0.1064
Case II : Optimized shape for $C_{D\ first\ car}$	0.2713	0.0638	0.0374	0.1701

Table 4.3 Pressure drag variation and viscous drag variation of the optimized model in case I when comparing with the base model

	First car	Last car
Pressure drag variation rate	+14.0%	-29.3%
Viscous drag variation rate	-2.3%	-3.4%

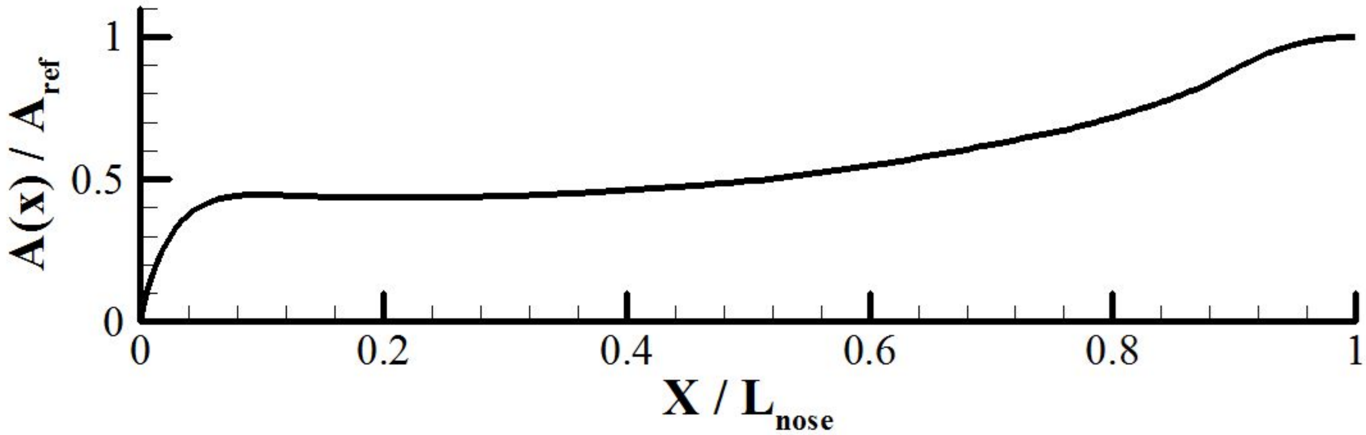

Fig. 4.1 Ku's optimal distribution of the cross-sectional area of high speed train nose to minimize the micro-pressure wave [2]

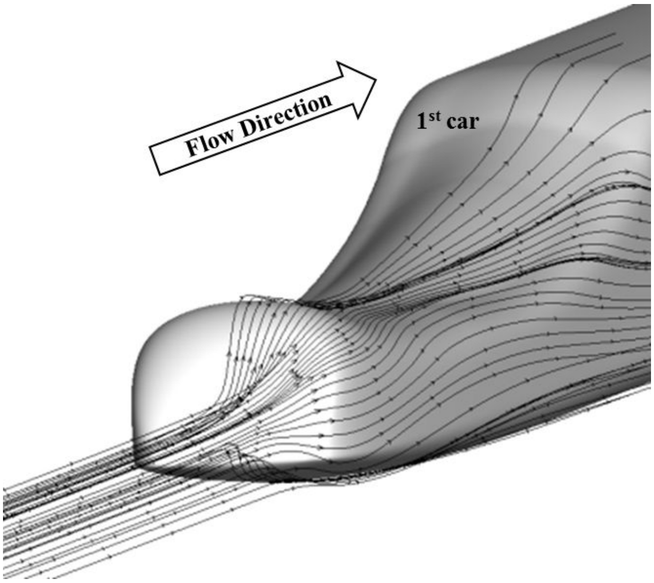

(a) Around the first car

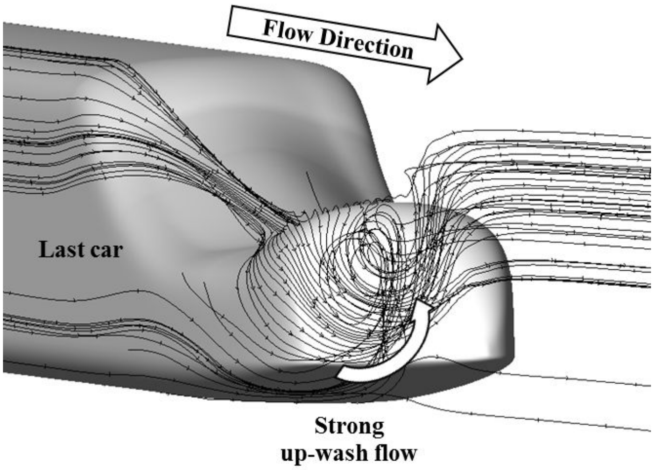

(b) Around the last car

Fig. 4.2 Numerically computed streamlines around the 3-car base model at V=500 km/h (at Re# = 3.36$\times 10^7$)

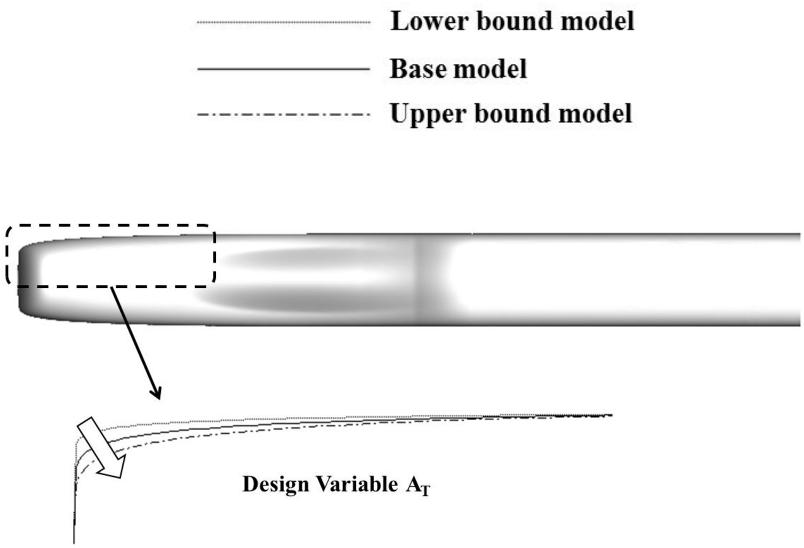

Fig. 4.3 Shape comparisons among the lower bound model, the base model, and the upper bound model of design variable A_T

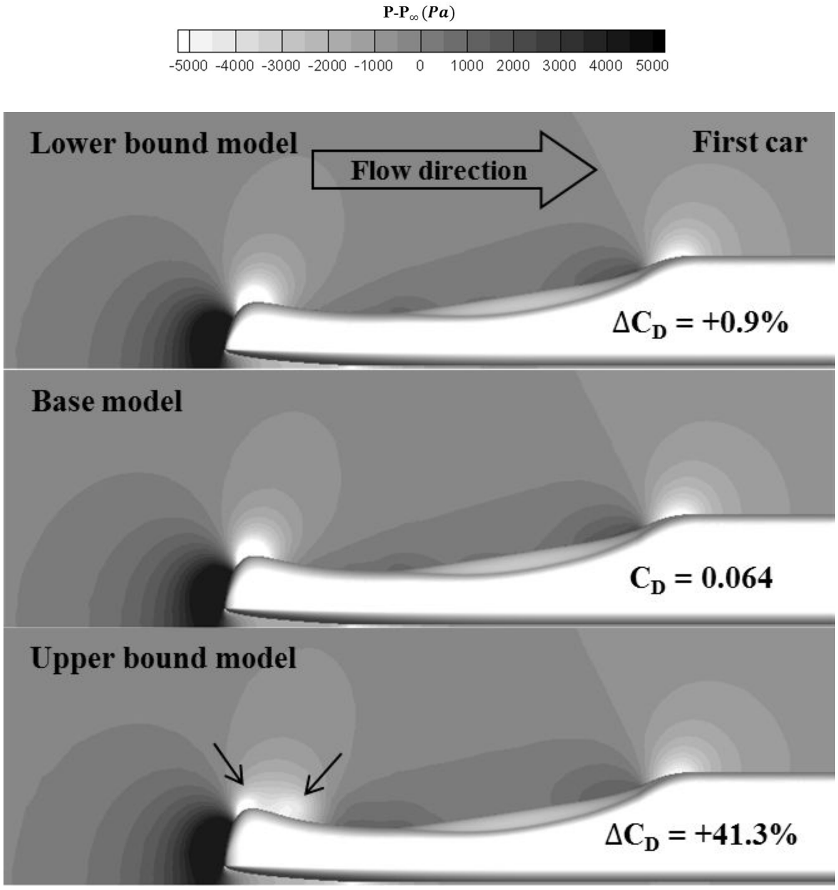

Fig. 4.4 Comparisons of pressure contours around the first car among the lower bound model, the base model, and the upper bound model of design variable A_T at Re# = 3.36×10^7

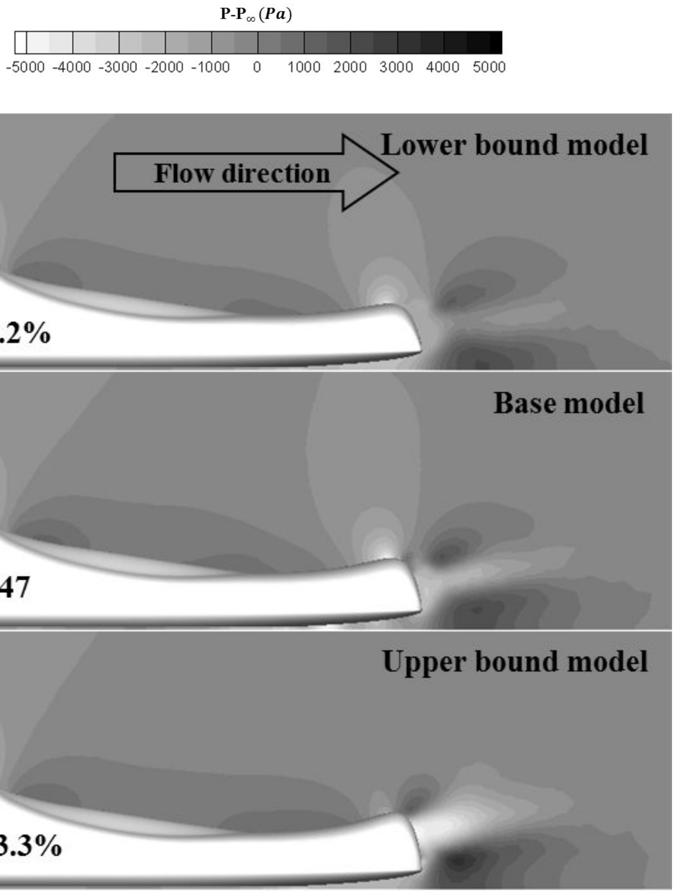

Fig. 4.5 Comparisons of pressure contours around the last car among the lower bound model, the base model, and the upper bound model of design variable A_T at Re# = 3.36×10^7

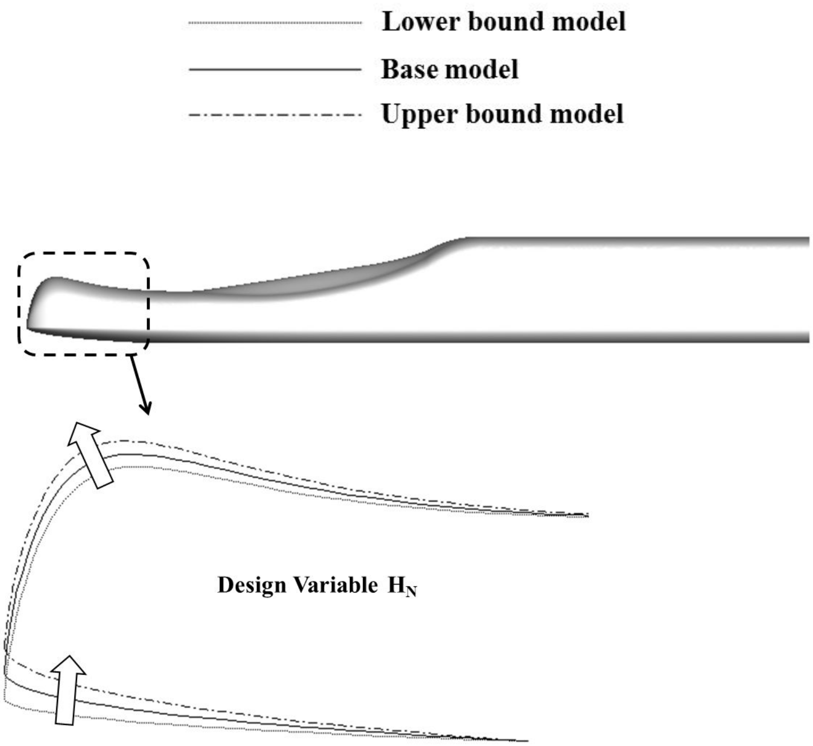

Fig. 4.6 Shape comparisons among the lower bound model, the base model, and the upper bound model of design variable H_N

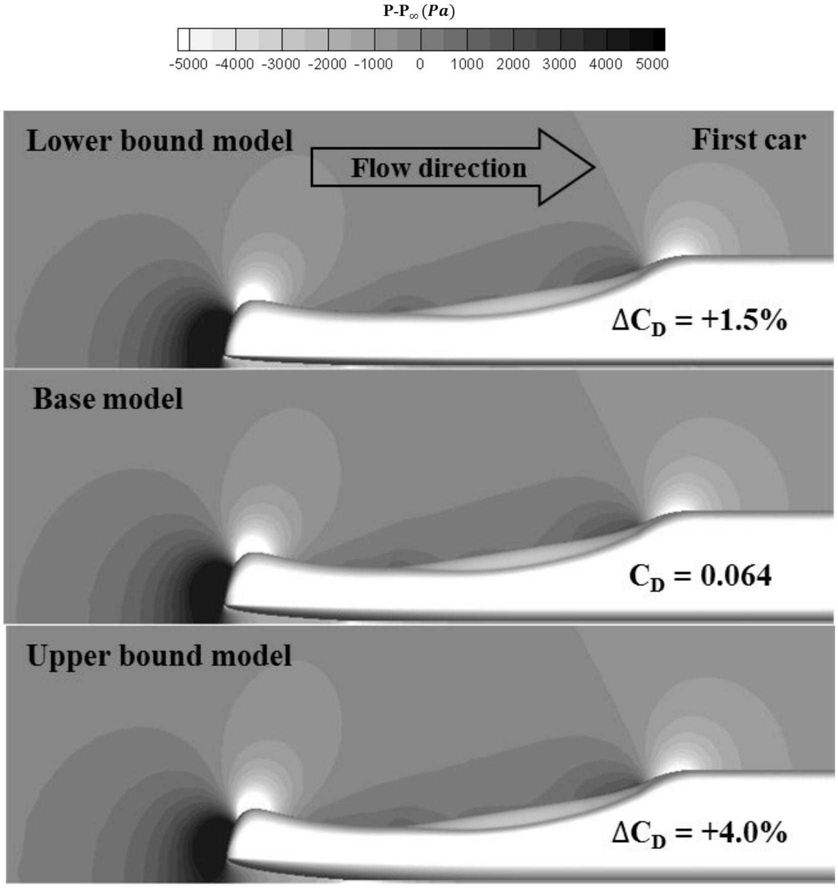

Fig. 4.7 Comparisons of pressure contours around the first car among the lower bound model, the base model, and the upper bound model of design variable H_N at Re# = 3.36×10^7

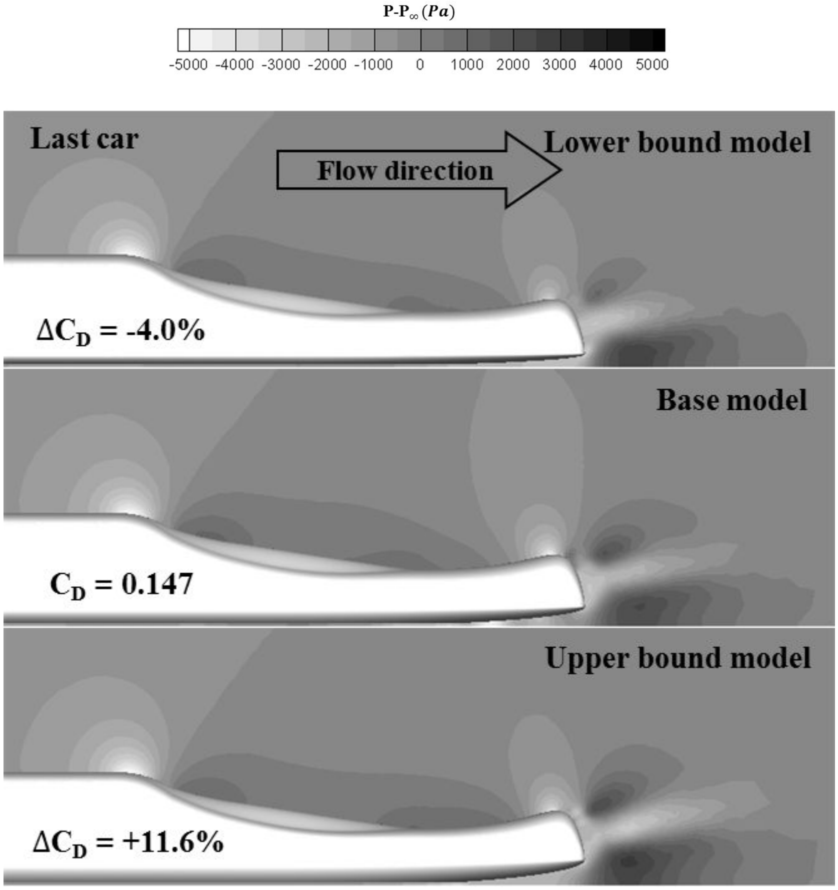

Fig. 4.8 Comparisons of pressure contours around the last car among the lower bound model, the base model, and the upper bound model of design variable H_N at Re# = 3.36×10^7

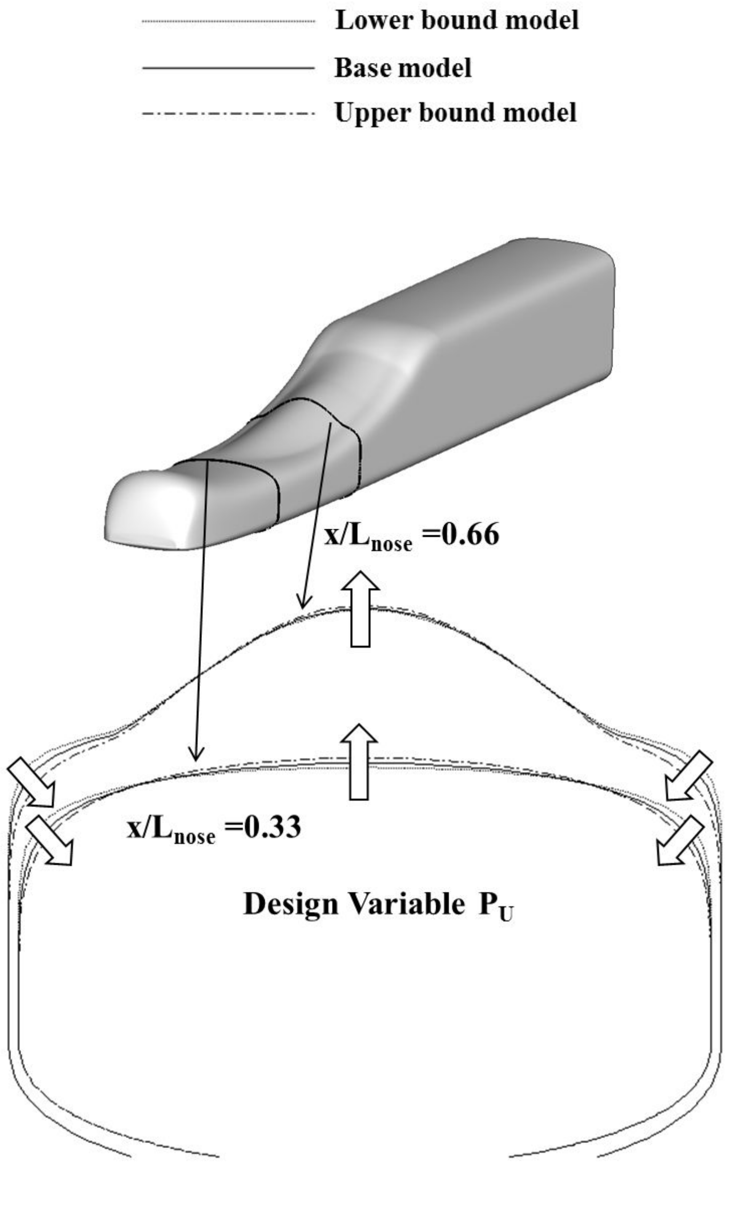

Fig. 4.9 Shape comparisons among the lower bound model, the base model, and the upper bound model of design variable P_U

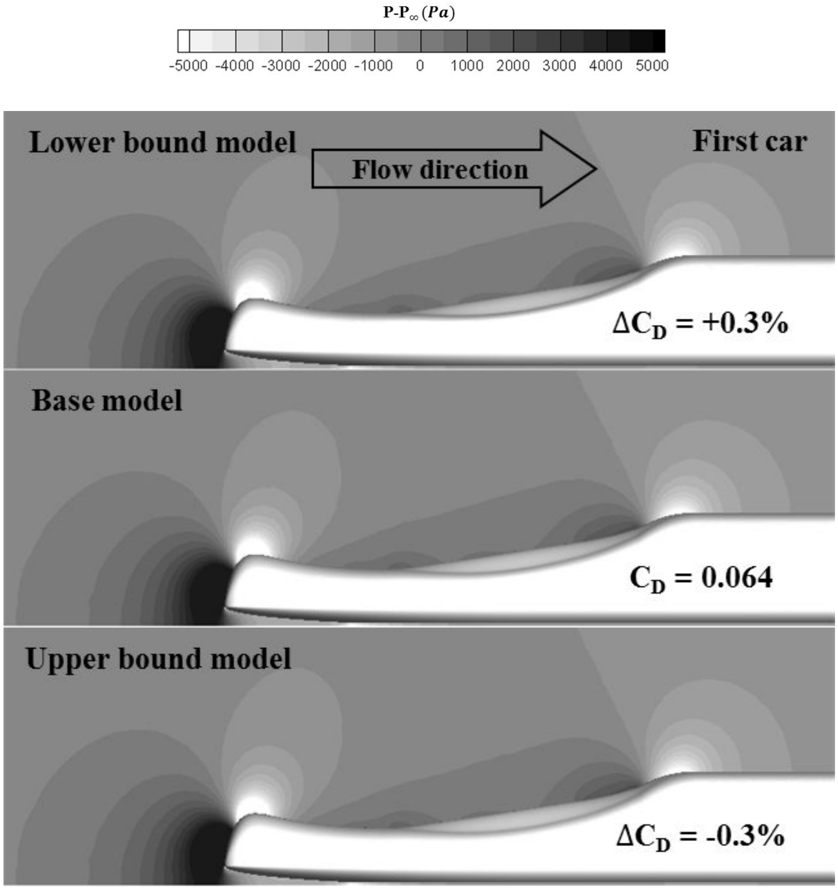

Fig. 4.10 Comparisons of pressure contours around the first car among the lower bound model, the base model, and the upper bound model of design variable P_U at Re# = 3.36×10^7

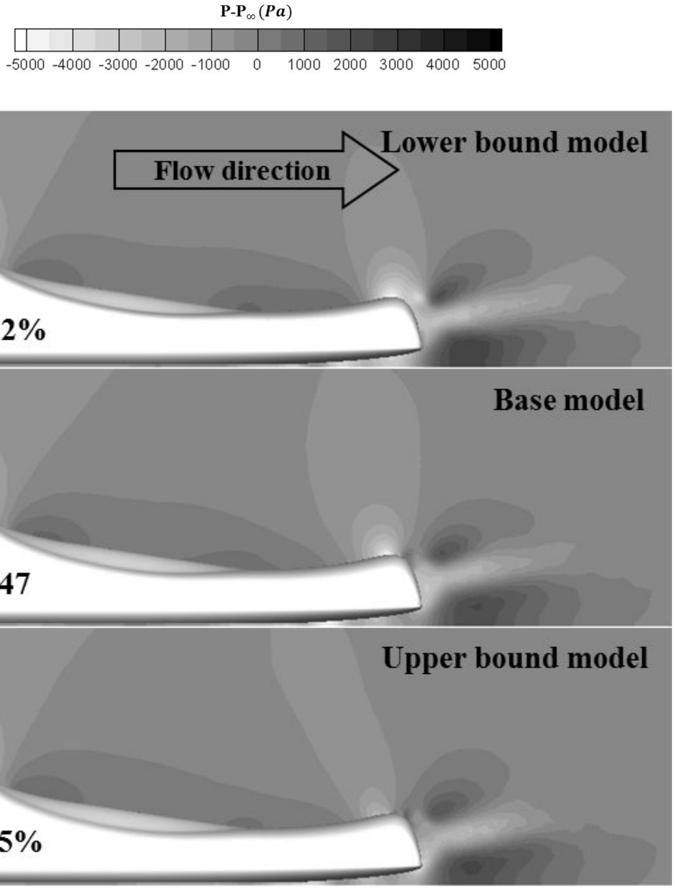

Fig. 4.11 Comparisons of pressure contours around the last car among the lower bound model, the base model, and the upper bound model of design variable P_U at Re# = 3.36×10^7

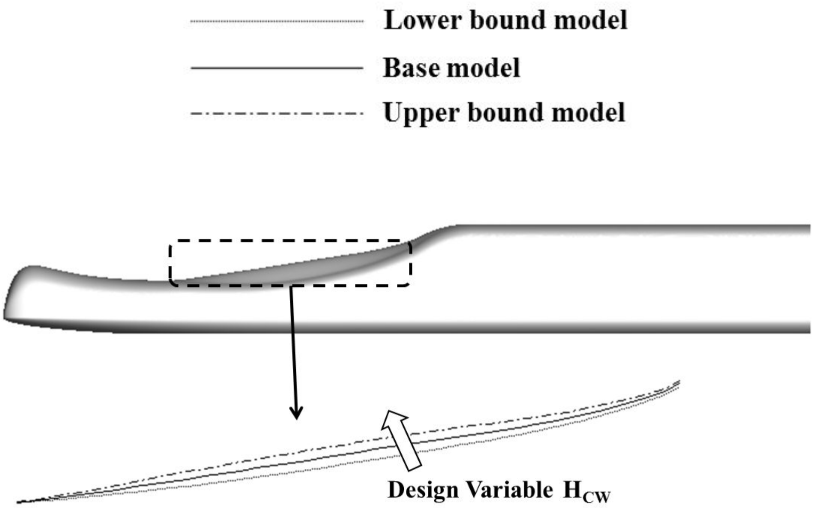

Fig. 4.12 Shape comparisons among the lower bound model, the base model, and the upper bound model of design variable H_{CW}

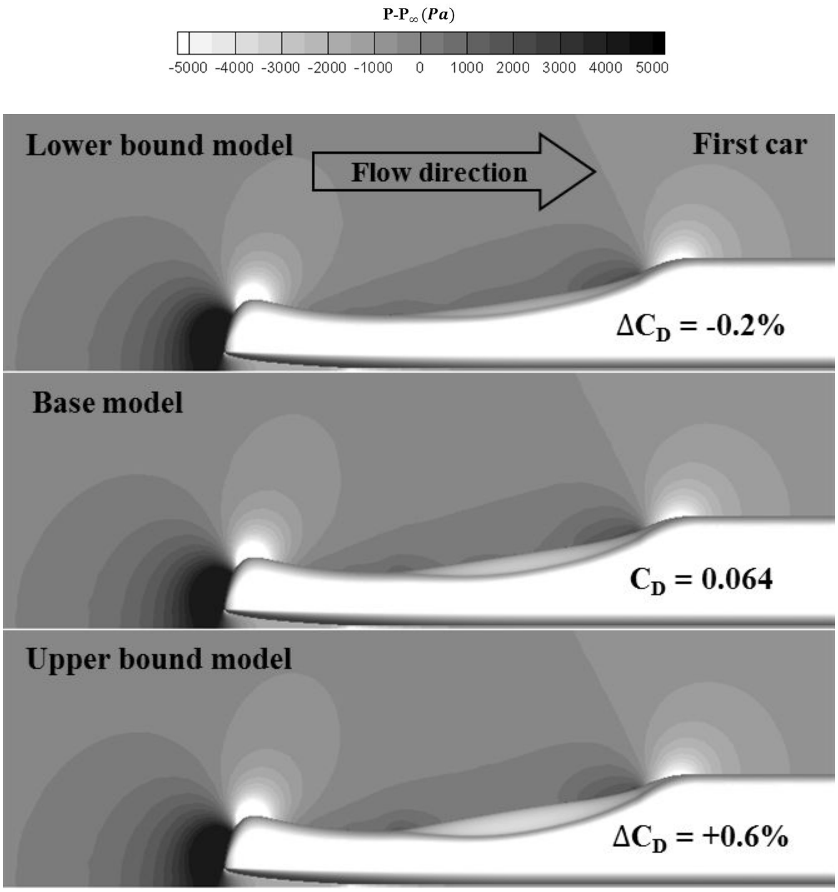

Fig. 4.13 Comparisons of pressure contours around the first car among the lower bound model, the base model, and the upper bound model of design variable H_{CW} at Re# = 3.36 × 10^7

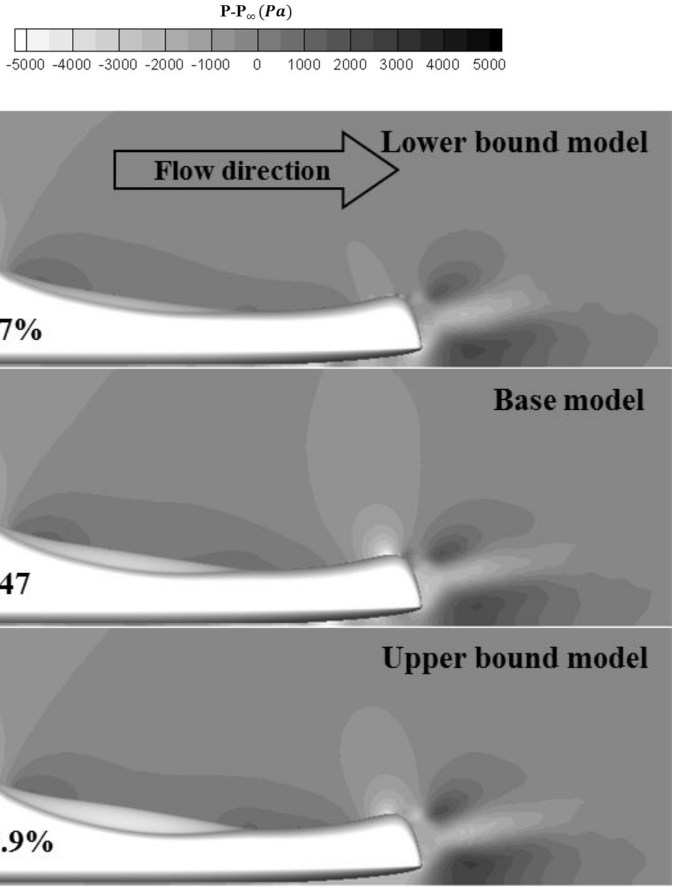

Fig. 4.14 Comparisons of pressure contours around the last car among the lower bound model, the base model, and the upper bound model of design variable H_{CW} at Re# = 3.36×10^7

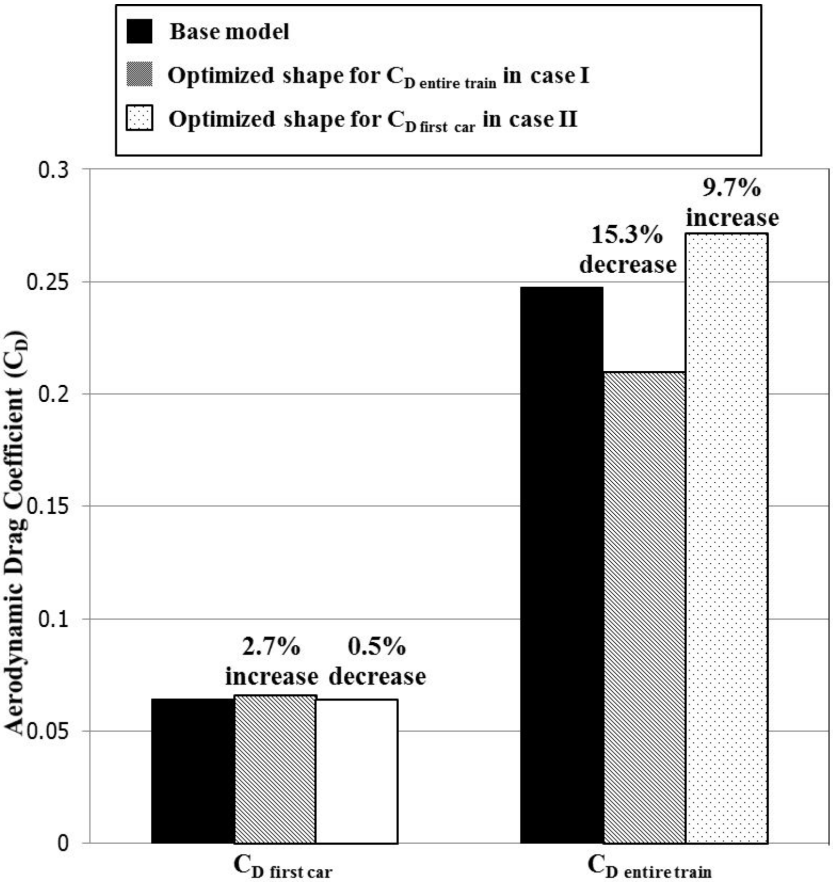

Fig. 4.15 Comparisons of drag coefficients between base model and the optimized shapes at V=500 km/h

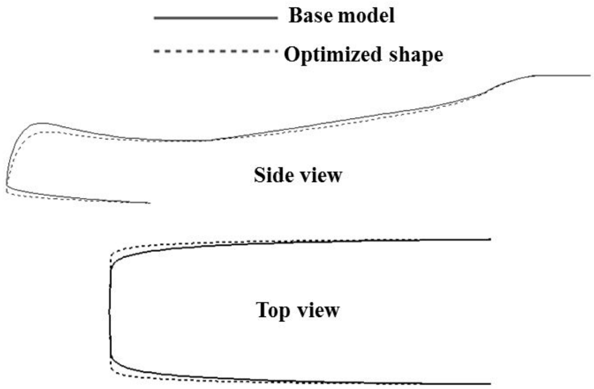

(a) Two-dimensional view

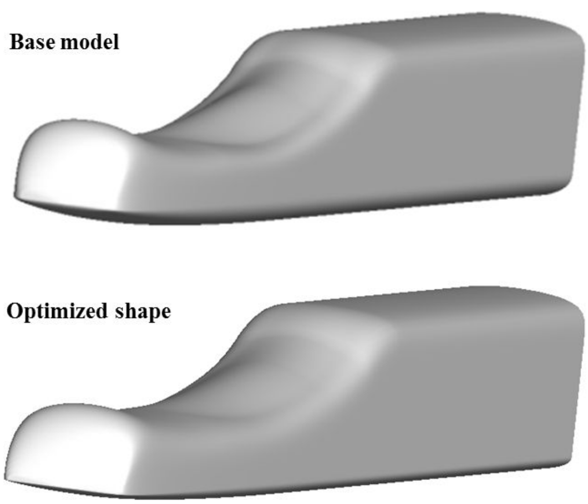

(b) Three-dimensional isometric view

Fig. 4.16 Comparison of model forms between of the base model and of the optimized shape for $C_{D\ \mathrm{entire\ train}}$ in case I

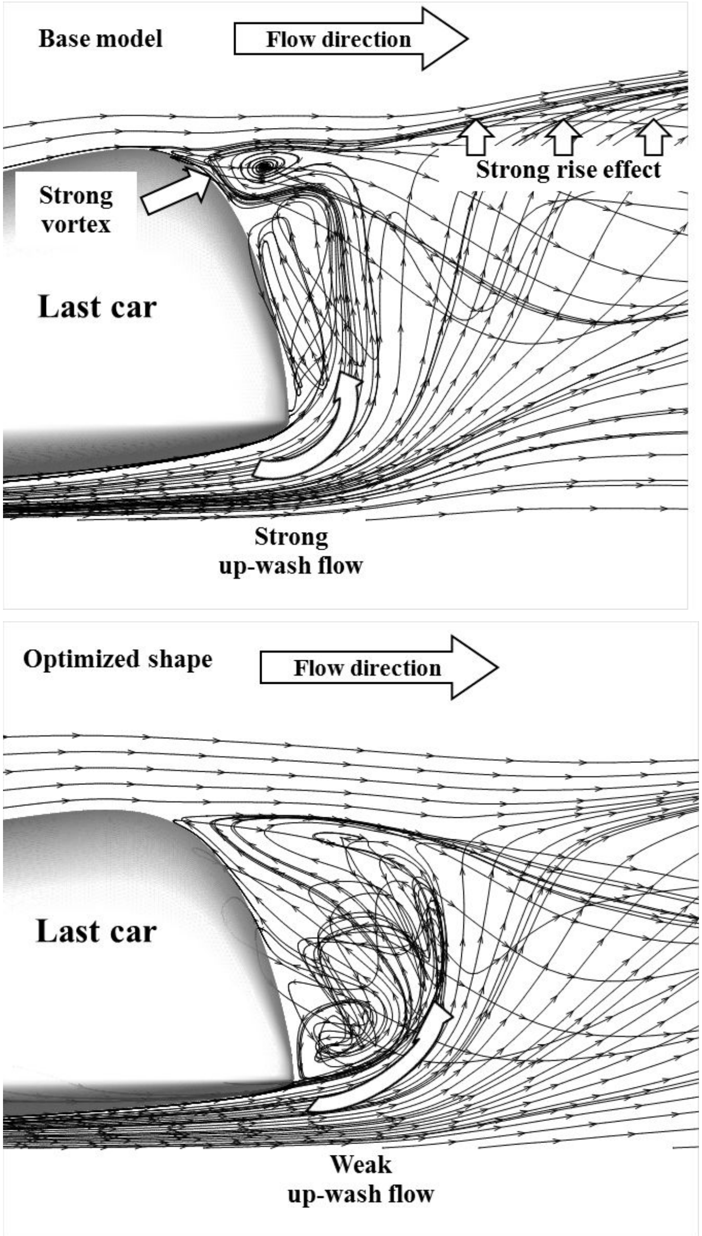

Fig. 4.17 Comparisons of streamline patterns behind the last car with the two-dimensional side view between the base model and the optimized shape for $C_{D\ \text{entire train}}$ in case I at Re# = 3.36×10^{7}

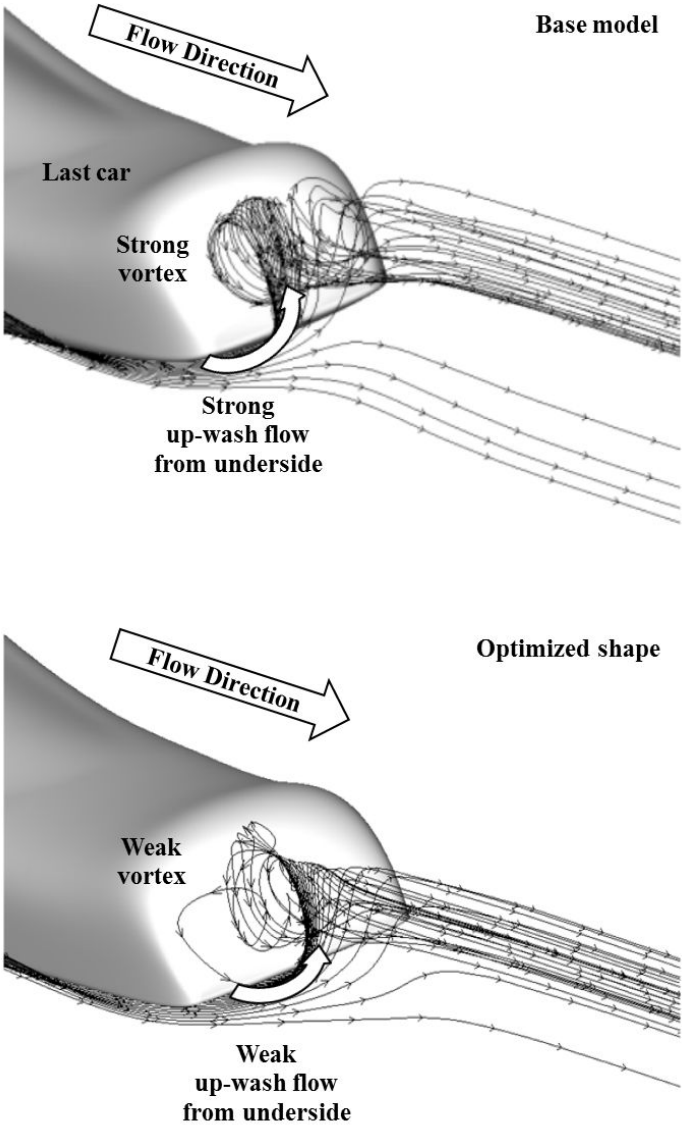

Fig. 4.18 Comparisons of streamline patterns from the underside of the last car between the base model and the optimized shape for $C_{D\ \mathrm{entire\ train}}$ in case I at Re# = 3.36×10^7

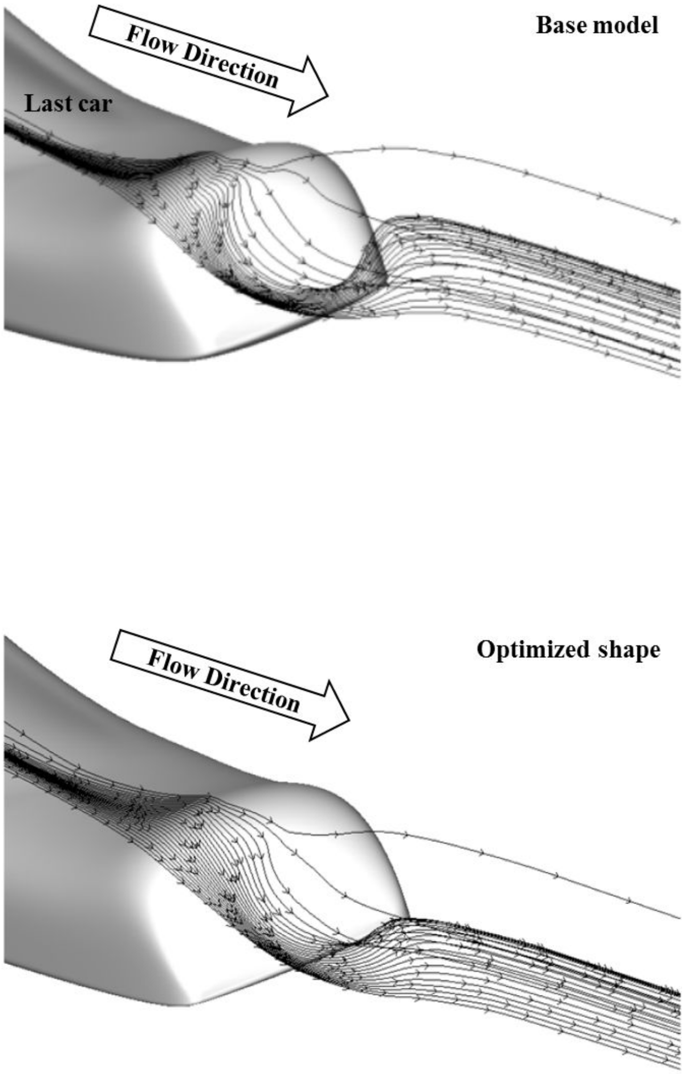

Fig. 4.19 Comparisons of streamline patterns from the upper side of the last car between the base model and the optimized shape for $C_{D\ entire\ train}$ in case I at Re# = 3.36×10^{7}

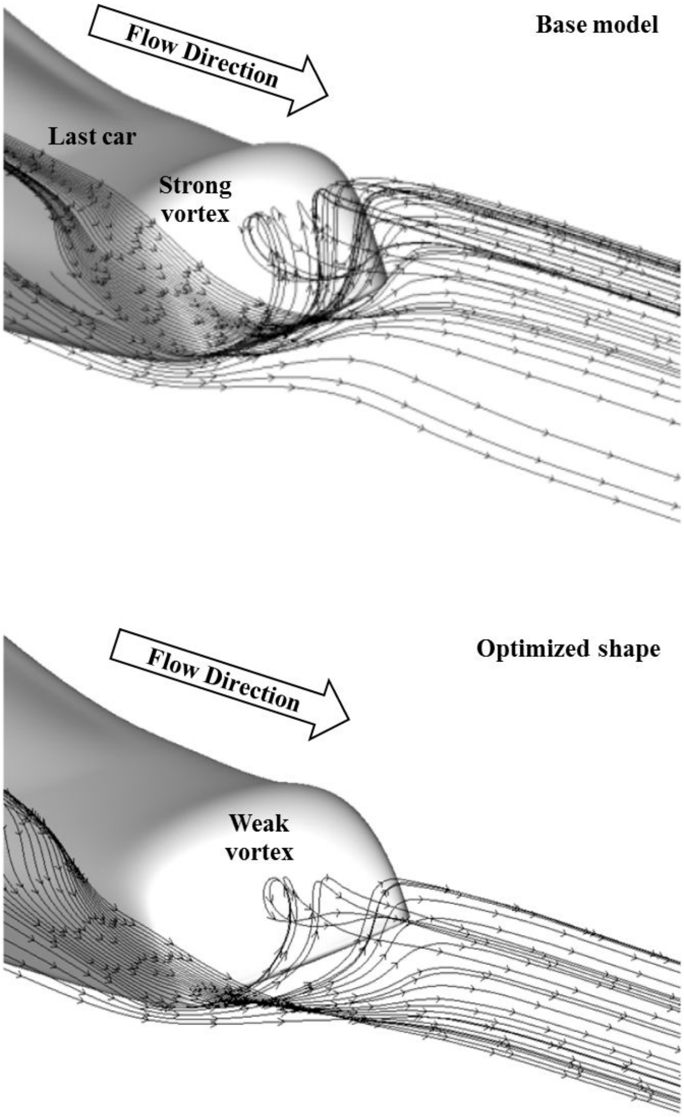

Fig. 4.20 Comparisons of streamline patterns from the middle side of the last car between the base model and the optimized shape for $C_{D\ entire\ train}$ in case I at Re# = 3.36×10^7

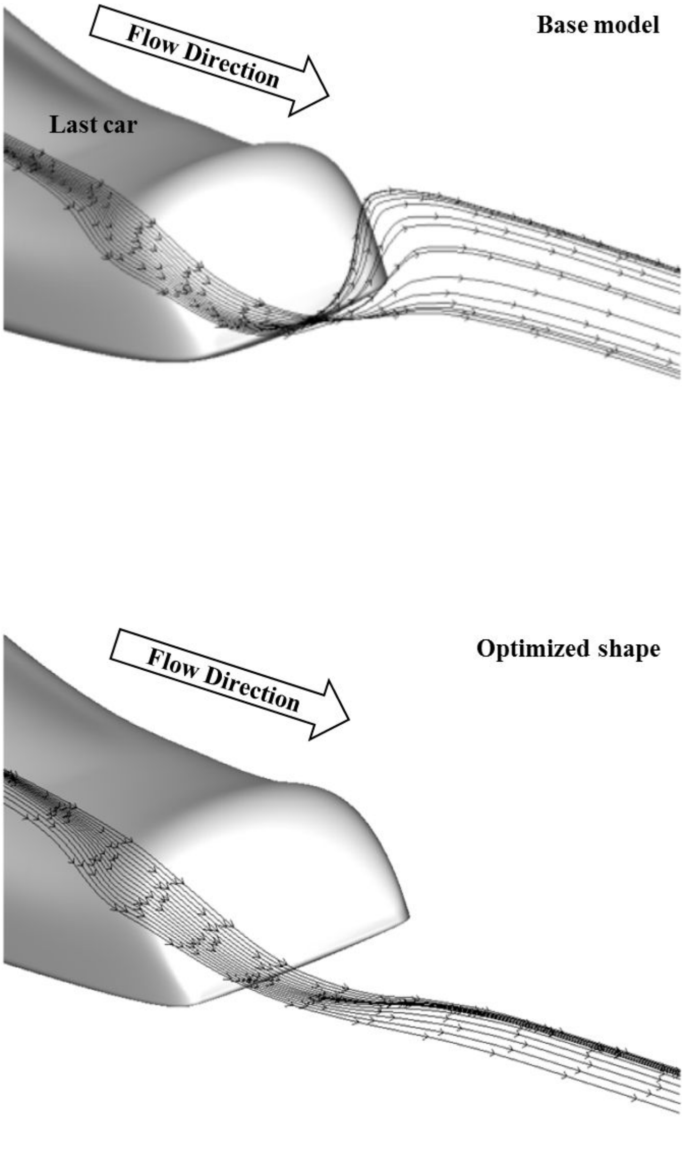

Fig. 4.21 Comparisons of streamline patterns from the shoulder side of the last car between the base model and the optimized shape for $C_{D\ entire\ train}$ in case I at Re# = 3.36×10^7

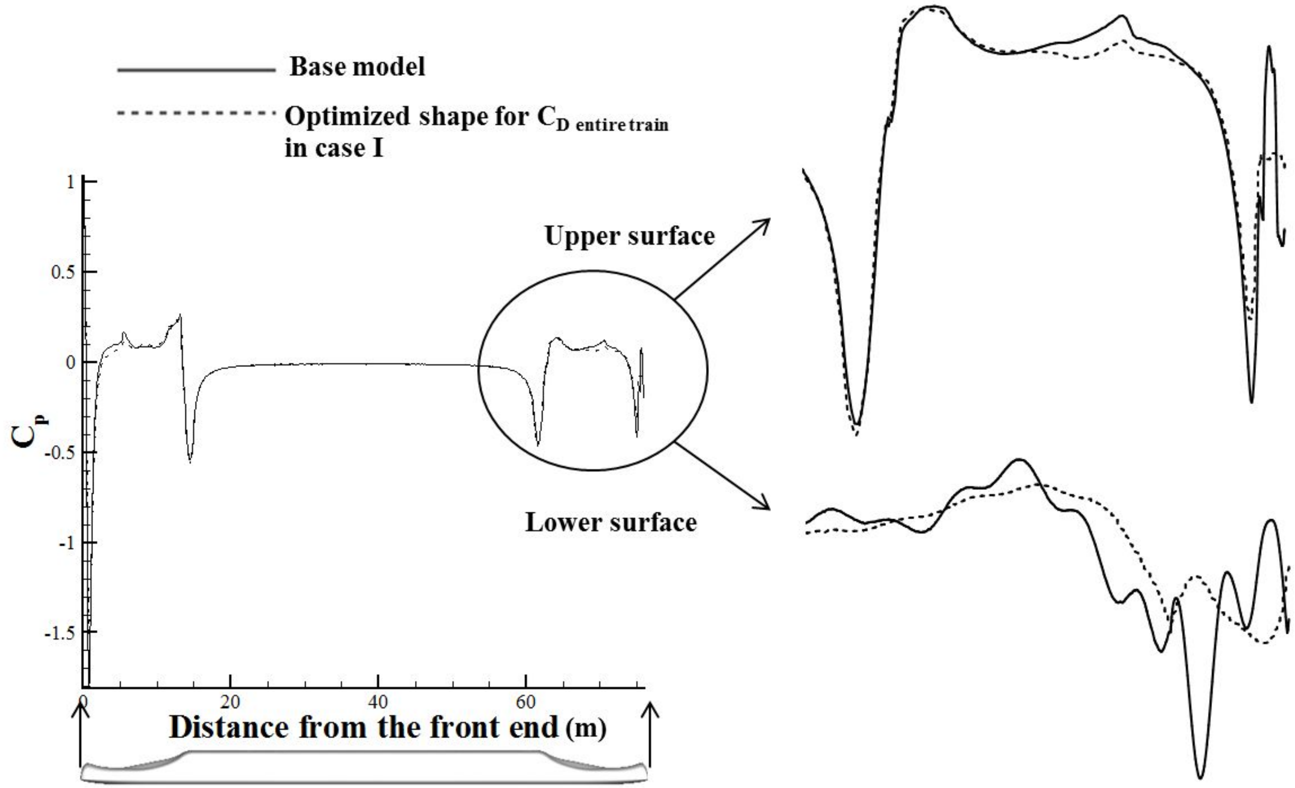

Fig. 4.22 Comparisons of pressure distributions at the symmetric lateral centerline surface

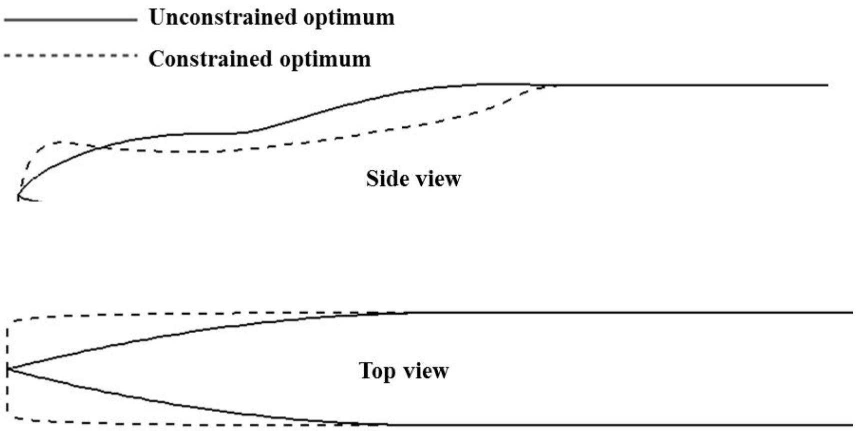

Fig. 4.23 Comparison of model forms between of the constrained optimum model and of the unconstrained optimum model from a 2D view

Chapter 5. Conclusion

The high-speed train uses two symmetrically corresponding shaped power cars at both ends. Consequently, the same nose shape plays a role as a leading part and a role as a trailing part in one train at the same time. Thus the existing model of the optimized first car nose shape which does not consider the entire train is not sound in terms of the aerodynamic drag. Therefore, it is necessary to consider the entire train including the first car nose and the last car nose and especially accurate simulation of the wake area for the optimization of the shape design of the three-dimensional symmetric train to reduce the total aerodynamic drag.

Two optimizations are performed with unconstrained models for one objective and under the constraint of the optimized cross-sectional area distribution for two objectives respectively. Both optimizations are performed for two cases. One is done for the reduction of the total aerodynamic drag and the other is done for the reduction of the aerodynamic drag of the first car only. The three-dimensional symmetric train body was constructed using the Vehicle Modeling Function, without any constraint for the unconstrained problem and with the optimum cross-sectional area distribution for the constrained optimization. The viscous compressible numerical simulations were performed with three-dimensional unstructured meshes.

In the unconstrained optimization, it was found that the total aerodynamic drag of the entire train with the optimized shape for the entire train is reduced by 5.8% when compared to the unconstrained base model, whereas that with the optimized shape for only the first car is changed. On the other hand, in the constrained optimization, the total aerodynamic drag was effectively reduced by 15.3 % when compared to that of the constrained base model while that with the optimized shape for only the first car is increased by 9.7%.

The low-risen and long vertical nose shape of the unconstrained optimum shape weakens the whirled flow around the nose tip. On the other hand, the low-risen and wide horizontal end shape of the constrained optimum shape weakens the up-wash flow and vortices behind the blunt nose. Both shape characteristics reduce the overall aerodynamic drag of each base model.

The three dimensional modeling is very necessary because the wake area has to be simulated as accurately as possible for design optimization of the actual front-rear symmetric train. Therefore, it can be said that the Vehicle Modeling Function is a valuable tool in that it enables the three-dimensional modeling of the train body efficiently with or without any constraint, leading to a successful three-dimensional shape optimization. It also can be concluded that considering both the first car nose and the last car nose at the same time is necessary for the effective optimization of the nose shape so as to minimize the total aerodynamic drag of the symmetric train.

References

[1] Raghu S. Raghunathan, H.-D. Kim, T. Setoguchi, "Aerodynamics of high-speed railway train," *Progress in Aerospace Sciences*, Vol. 38, 2002, pp. 469-514.

[2] Yo-cheon Ku, Joo-Hyun Rho, Su-Hwan Yun, Min-Ho Kwak, Kyu-Hong Kim, Hyeok-Bin Kwon, and Dong-Ho Lee, "Optimal cross-sectional area distribution of a high speed train nose to minimize the tunnel micro-pressure wave," *Structural and Multidisciplinary Optimization*, Vol. 42, No. 6, 2010, pp. 965-976.

[3] Su-Hwan Yun, Min-Ho Kwak, Dong-Ho Lee, Hyeok-Bin Kwon, and Tae-Hwan Ko, "Passive reduction of large pressure variation for a high-speed express train in a narrow tunnel using an extra dummy tunnel duct," *Journal of Mechanical Science and Technology*, Vol. 24, No. 7, 2010, pp. 1433-1440.

[4] Jaeho Hwang and Dong-Ho Lee, "Unsteady Aerodynamic Loads on High Speed Train Passing by Each Other," *KSME International Journal*, Vol. 14, No. 8, 2000, pp. 867-878.

[5] Chris Baker, "The flow around high speed trains," *Journal of Wind Engineering and Industrial Aerodynamics*, Vol. 98, No.(6-7), 2010, pp. 277-298.

[6] Yeongbin Lee, Joohyun Rho, Kyu Hong Kim, and Dong-Ho Lee, "Fundamental studies on free stream acceleration effect on drag force in bluff bodies," *Journal of Mechanical Science and Technology*, Vol. 25, No. 3, 2011, pp. 279-285.

[7] Tae-yoon Kim, Bo-sung Lee, and Dong-ho Lee, "Study on the Unsteady Wakes Past a Square Cylinder near a Wall," *KSME International Journal*, Vol. 19, No. 5, 2005, pp. 1169-1181.

[8] Moon-Sang Kim, Byung-Woo Jeon, Yong-Nyun Kim, Hyeok-Bin Kwon, and Dong-Ho Lee, "An Implementation of the Robust Inviscid Wall Boundary Condition in High-Speed Flow Calculatons," *KSME International Journal*, Vol. 15, No. 5, 2001, pp. 671-680.

[9] C.J. Baker, "Flow and Dispersion in Ground Vehicle Wakes," *Journal of Fluids and Structures*, Vol. 15, No. 7, 2001, pp. 1031-1060.

[10] J.L. Peters, "Optimizing Aerodynamics to Raise IC Performance," *Railway Gazette International*, 1982, pp. 817-819.

[11] B P Rochard and F Schmid, "A review of methods to measure and calculate train resistances," *Journal of Rail and Rapid Transit*, Vol. 214, No. 4, 2000, pp. 185-199.

[12] S. Ozawa and T. Maeda, "Model Experiment on Reduction of Micro-Pressure Wave Radiated from Tunnel Exit," *JSME International Symposium on Scale Modeling*, JSME, Tokyo, 1988.

[13] T. Maeda, T. Matsumura, M. Iida, K. Nakatani, and K. Uchida, "Effect of Shape of Train Nose on Compression Wave Generated by Train Entering Tunnel," *The International Conference on Speedup Technology for Railway and Maglev Vehicles*, JSME, Yokohama, 1993.

[14] K.H. Han, J.S. Park, "Aerodynamic running characteristics of a high speed train," *1999 KSNVE Annual Spring Conference*, KSNVE, Seoul, 1999, pp. 108-113.

[15] Seoul National University, "A research project report on the Aerodynam-

ic Technology Advancement of the High-Speed EMU," SNU Aerospace Vehicle Design Lab., Seoul, Sep. 2011.

[16] S. Hosaka, M. Sugesawa, H. Tsunoda, and K. Yamamoto, "Improvements on new "MLX01" vehicles of the JR Maglev – Aerodynamic characteristics," *World Congress on Railway Research*, Edinburgh, 2003, pp. 523-530.

[17] Minho Kwak, Yeongbin Lee, Junguk Lee, Junho Cho, Kyuhong Kim, and Dongho Lee, "Experimental Study on Aerodynamic Drag Characteristics by Train Underbody Shape Variation," *30th AIAA Applied Aerodynamics Conference*, AIAA, New Orleans, 2012.

[18] Atsushi Ido, Yoshihiko Kondo, Tsuyoshi Matsumura, Minoru Suzuki, and Tatsuo Maeda, "Wind Tunnel Tests to Reduce Aerodynamic Drag of Trains by Smoothing the Under-floor Construction," *Quarterly Report of RTRI*, Vol. 42, No. 2, 2001, pp. 94-97.

[19] Giampaolo Mancini, Antonio Malfatti, Angelo G. Violi, and Gerd MAtschke, "Effects of experimental bogie fairings on the aerodynamic drag of the ETR 500 high speed train," *World Congress on Railway Research*, KolnMesse, 2001.

[20] Hyeok-bin Kwon, Dong-ho Lee, and Je-hyun Baek, "An Experimental Study of Aerodynamic Drag on High-speed Train," *KSME International Journal*, Vol. 14, No. 11, 2000, pp. 1267-1275.

[21] Y. Wakabayashi, T. Kurita, H. Yamada, and M. Horiuchi, "Noise measurement results of Shinkansen high-speed test train (FASTECH 360S,Z)," *Proceedings of 9th International Workshop on Railway Noise*, Munich, 2007.

[22] M Ito, "Improvement to the aerodynamic characteristics of Shinkansen

rolling stock," *Journal of Rail and Rapid Transit*, Vol. 214, No. 3, 2000, pp. 135-143.

[23] Guowei Yang, "Aerodynamic Design on China New High-Speed Trains," *Proceedings of the 1st International Workshop on High-Speed and Intercity Railways*, Hong Kong Polytechnic University, Hong Kong, 2012.

[24] K. Cui, X.P. Wang, S.C. Hu, T.Y. Gao, and Guowei Yang, "Shape Optimization of High-Speed Train with the Speed of 500kmh," *Proceedings of the 1st International Workshop on High-Speed and Intercity Railways*, Hong Kong Polytechnic University, Hong Kong, 2012.

[25] Ch. Heine and G. Matschke, "The Influence of the Nose Shape of High-Speed Trains on the Aerodynamic Coefficients," *World Congress on Railway Research*, Koln, 2001.

[26] M.J. Siclari, R. Endo, and G. Carpenter, "The Application of Navier-Stokes Computations to the Design of High-Speed, Low-Drag Magnetically Levitated (MAGLEV) Vehicle Shapes," *13th Applied Aerodynamics Conference*, San Diego, 1995, pp. 1189-1207.

[27] Hassan Hemida and Sinisa Krajnovic, "LES study of the influence of the nose shape and yaw angles on flwo structures around trains," *Journal of Wind Engineering and Industrial Aerodynamics*, Vol. 98, No.1, 2010, pp. 34-46.

[28] E. Lorriaux, N. Bourabaa, and F. Monnoyer, "Aerodynamic Optimization of Railway Motor Coaches," *World Congress on Railway Research*, Montreal, 2006.

[29] S. Krajnovic, "Improvement of aerodynamic properties of high-speed trains by shape optimization and flow control," *World Congress on Rail-*

way Research, Seoul, 2008.

[30] V.V. Vytla, P.G. Huang, and R.C. Penmetsa, "Multi Objective Aerodynamic Shape Optimization of High Speed Train Nose Using Adaptive Surrogate Model," *28th AIAA Applied Aerodynamic Conference*, Chicago, 2010.

[31] Hyeok-bin Kwon, Yu Shin Kim, Dong-ho Lee, and Moon sang Kim, "Nose Shape Optimization of the High-speed Train to Reduce the Aerodynamic drag and Micro-pressure Wave," *Proceeding of Spring Conference of The Korean Society for Mechanical Engineering*, 2001, pp. 373-379.

[32] Yocheon Ku, "Two-Step Multi-Objective Nose Shape Optimization of a High-Speed Train using the Vehicle Modeling Function," Ph.D. Dissertation, Mechanical and Aerospace Engineering Dept., Seoul National University, Seoul, 2009.

[33] Yo-Cheon Ku, Min-Ho Kwak, Hoon-Il Park, and Dong-Ho Lee, "Multi-Objective Optimization of High-Speed Train Nose Shape Using the Vehicle Modeling Function," *48th AIAA Aerospace Sciences Meeting*, AIAA, Orlando, 2010.

[34] Minho Kwak, Suhwan Yun, Yeongbin Lee, Hyeokbin Kwon, Kyuhong Kim, and Dongho Lee, "Optimum Nose Shape of a Fron-Rear Symmetric Train for the Reduction of the Total Aerodynamic Drag," *Journal of Mechanical Science and Technology*, (to be published).

[35] Fluent Inc., *Fluent 6.3 User's Guide*, Lebanon, 2006.

[36] P. K. Sweby, "High resolution TVD schemes using flux limiters," *Lectures in Applied Mathematics*, Vol. 22, 1985, pp. 289-309.

[37] Stuart E. Rogeres and Dochan Kwak, "Upwind Differencing Scheme for

the Time-Accurate Incompressible Navier-Stokes Equations," *AIAA Journal*, Vol. 28, No. 2, 1990, pp. 253-262.

[38] B.M. Kulfan and J.E. Bussoletti, "Fundamental Parametric Geometry Representations for Aircraft Component Shapes," *11th AIAA/ISSMO Multidisciplinary Analysis and Optimization Conference*, AIAA, Portsmouth, 2006.

[39] B.M. Kulfan, "Universal Parametric Geometry Representation Method – CST," *45th AIAA Aerospace Sciences Meeting and Exhibit*, AIAA, Reno, 2007.

[40] Joo-Hyun Rho, Yo-Cheon Ku, Jung-Do Kee, and Dong-Ho Lee, "Development of a Vehicle Modeling Function for Three-Dimensional Shape Optimization," *Journal of Mechanical Design*, Vol. 131, No. 12, 2009.

[41] Y.C. Ku, J.H. Rho, S.H. Yun, M.H. Kwak and D.H. Lee, "A Study of Design Method for Train Nose Shape Using Configuration Function," *2008 Spring Conference of Korean Society for Railway*, KSR, Daegu, 2008 (in Korean).

[42] M.D. McKay, R.J. Beckman, and W.J. Conover, "A Comparison of Three Methods for Selecting Values of Input Variables in the Analysis of Output from a Computer Code," *Technometrics*, Vol. 21, 1979, pp. 239–245.

[43] J. Sacks, W. Welch, T.J. Mitchell, and H.P. Wynn, "Design and Analysis of Computer Experiments," *Stat. Sci.*, Vol. 4, 1989, pp. 409-435.

[44] M.E. Johnson, L.M. Moore, and D. Ylvisaker, "Minimax and Maximin Distance Designs," *Journal of Statistical Planning and Inference*, Vol. 26, No. 2, 1990, pp. 131-148.

[45] V. Roshan Joseph and Ying Hung, "ORTHOGONAL-Maximin Latin

Hypercube Designs," *Statistica Sinica*, Vol. 18, 2008, pp. 171-186.

[46] Sangook Jun, Yong-Hee Jeon, JeongHwa Kim, and Dong-ho Lee, "Application of the Robust and Reliability-Based Design Optimization to the Aircraft Wing Design," *Journal of the Korean Society for Aeronautical and Space Sciences*, Vol. 34, No. 8, 2006, pp. 24-32 (in Korean).

[47] S.O. Kang, S.O. Jun, K.H. Park, Y.H. Jeon, and D.H. Lee, "Study of Neural Network Training Algorithm Comparison and Prediction of Unsteady Aerodynamic Forces of 2D Airfoil," *Journal of the Korean Society for Aeronautical and Space Science*, Vol. 27, No.5, 2009, pp. 425-423 (in Korean).

[48] J.A. Freeman and D.M. Skapura, *Neural Networks Algorithm, Applications, and Prgoramming Techniques*, Addison-Wesley Publishing Company, Boston, 1992.

[49] G. N. Vanderplaats, *Numerical Optimization Techniques for Engineering Design*, 3rd ed., Vanderplaats Research & Development Inc, Colorado Springs, 1999.

[50] H. B. Kwon, Y. H. Park, D. H. Lee, and M. S. Kim, "Wind tunnel experiments on Korean high speed trains using various ground simulation techniques," *Journal of Wind Engineering and Industrial Aerodynamics*, Vol. 89, 2001, pp. 1179-1195.

[51] Seung-On Kang, "Design Optimization and Active Flow Control for Automotive Aerodynamic Drag Reduction," Ph.D. Dissertation, Mechanical and Aerospace Engineering Dept., Seoul National University, Seoul, 2011.

[52] C.H. Liu, Dilong Guo, Shuanbao Yao, and Guowei Yang, "The Influence of Different Cross-Section Shapes of Train Body on Aerodynamic Perfor-

mance," *Proceedings of the 1st International Workshop on High-Speed and Intercity Railways*, Hong Kong Polytechnic University, Hong Kong, 2012.

초 록

레일 위를 주행하는 고속열차의 경우 같은 형상의 동력차가 동시에 앞과뒤 차량으로 방향만 바뀌어서 사용된다. 그러므로 첫번째 차량의 위치에만 적합하게 설계된 이전의 최적 전두부 형상은 마지막 차량의 위치에 있을 때 전체 공기저항의 관점에서 적합하지 않다. 또한 3차원 형상 최적설계에 있어 정확한 후류 모사는 매우 중요한 부분이지만, 이전 연구들의 열차 후류 모사는 열차 형상과 경계조건으로 인해 정확하지 않았다. 그러므로 전체 공기저항을 최소화하는 관점에서의 3차원 전두부 형상 최적설계는 전체 차량 형상을 모두 고려해야 하며, 특히 후미부에서의 후류 영역을 제대로 모사하는 것이 필요하다.

본 연구에서는 전체 공기저항을 줄이기 위한 전후대칭열차의 전두부 3차원 형상 최적설계를 수행하였다. 전체 공기저항을 줄이는 비제약 최적설계와 전체공기저항과 미기압파를 모두 저감하기 위해 미기압파를 최소화하는 전두부 단면적 분포를 제약조건으로 가지면서 전체공기저항을 저감하는 제약모델 최적설계를 각각 수행하였다. Vehicle Modeling Function을 이용하여 3차원 열차 형상을 구성하였고, Navier-Stokes 방정식과 비정렬격자를 이용하여 그 공기저항을 예측하였다. 전체공기저항을 고려한 경우와 첫번째 차량의 공기저항만을 고려한 경우의 최적설계를 비제약 최적설계와 제약모델 최적설계 모두의 경우에 각각 수행하였다. Maxi-min Latin Hypercube Sampling 방법을 이용하여 추출한 실험점을 바탕으로 인공신경망을

구성하여 최적설계에 이용하였다.

비제약 최적설계의 경우, 베이스형상과 비교했을 때, 전체공기저항을 고려한 전두부 형상을 적용한 열차모델은 전체공기저항이 약 5.8% 감소하였고, 첫번째 차량의 공기저항만 고려한 전두부 형상을 적용한 열차 모델은 전체공기저항의 감소가 미미하였다. 제약모델 최적설계의 경우, 베이스형상과 비교했을 때, 전체공기저항을 고려한 전두부 형상을 적용한 열차모델은 전체공기저항이 약 15.3% 감소하였고, 첫번째 차량의 공기저항만 고려한 전두부 형상을 적용한 열차 모델은 전체공기저항이 오히려 9.7% 증가하였다.

비제약설계 최적 전두부 형상의 낮게 깔리면서 세로로 긴 형상특징은 열차 뒤쪽 전두부 끝단 근처의 회전유동을 약화시킨다. 반면에 제약모델기반 최적 전두부 형상의 낮게 깔리면서 가로로 긴 형상 특징은 열차 뒤쪽 전두부 아랫면에서 올라오는 유동과 그로 인해 형성되는 와류를 약화시킨다. 이런 두 최적형상의 형상특징들이 전체 공기저항을 감소시킨다.

실제 전후대칭열차의 최적설계를 위해서 후류 영역이 정확하게 모사되어야 하기 때문에 3차원 형상 모델링은 필수적이다. 그러므로 Vehicle Modeling Function은 3차원형상을 함수화하여 다양한 형상을 표현하는데 제약이 없기 때문에 형상제약조건의 유무에 관계없이 성공적인 3차원 형상 최적설계를 가능하게 하는 가치있는 도구이다. 또한 전체 공기저항을 줄이기 위한 효과적인 최적설계를 위해서는 앞뒤에서 방향만 다른 같은 전두부 형상의 양방향 주행을 모두 고려하는 것이 꼭 필요하다.

주요어: 전후 대칭 형상, 3차원 전두부 형상, 후류 모사, 열차 차체 모델링 함수, 공기저항, 최적설계

학 번 : 2006-23068